Low-Frequency Stabilizations of the PMCHWT Equation for Dielectric and Conductive Media: On a Full-Wave Alternative to Eddy-Current Solvers

Low-Frequency Stabilizations of the PMCHWT Equation for Dielectric and Conductive Media: On a Full-Wave Alternative to Eddy-Current Solvers

Viviana Giunzioni, *Member, IEEE*, Alberto Scazzola, *Member, IEEE*, Adrien Merlini, *Senior Member, IEEE*, and Francesco P. Andriulli, *Fellow, IEEE*

***Abstract*—We propose here a novel stabilization strategy for the Poggio–Miller–Chang–Harrington–Wu–Tsai (PMCHWT) equation that cures its frequency- and conductivity-related instabilities and is obtained by leveraging quasi-Helmholtz projectors. The resulting formulation is well-conditioned in the entire low-frequency regime, including the eddy-current one, and can be applied to arbitrarily penetrable materials, ranging from dielectric to conductive ones. In addition, by choosing the rescaling coefficients of the quasi-Helmholtz components appropriately, we prevent the typical loss of accuracy occurring at low frequency in the presence of inductive and capacitive type magnetic frill excitations, commonly used in circuit modeling to impose a potential difference. Finally, because it relies on quasi-Helmholtz projectors instead of the standard loop-star decomposition, our formulation can be used for modeling multiply connected geometries, without incurring the computational overhead caused by the search for the global loops of the structure, while also being compatible with most fast solvers. The efficacy of the proposed preconditioning scheme when applied to both simply and multiply connected geometries is corroborated by numerical examples.**

***Index Terms*—Eddy currents, full-wave, multiply connected, preconditioning, quasi-Helmholtz decomposition.**

I. Introduction

THE electromagnetic modeling of dielectric penetrable objects is crucial in a variety of applications, ranging from antenna design to micro- and nano-electronic applications [1], [2]. The boundary element method (BEM) allows to recast this problem in a set of integral equations [3]. Differently from other popular techniques, its use automatically enforces radiation conditions and only requires the discretization of surfaces separating different materials [3], [4]. These characteristics make the BEM one of the most favorable and widespread tools to numerically solve the electromagnetic scattering problem.

The Poggio–Miller–Chang–Harrington–Wu–Tsai (PMCHWT) equation [5] and the Müller equation [6] are among the most common integral formulations for penetrable bodies, and are, respectively, of the first- and second-kind. In spite of its favorable stability properties, the Müller equation in its standard, nonconforming, discretization has been shown to yield less accurate results than the PMCHWT formulation, especially in high-contrast scenarios [7], [8], [9]. Unfortunately, because of its first-kind nature, the PMCHWT formulation suffers from a dense-discretization ill-conditioning [10], [11]. In addition, the PMCHWT equation is also plagued by a severe low-frequency breakdown [10], [12], coupled to further instabilities related to the conductivity characterizing the obstacle medium.

To circumvent these issues, *ad hoc* solvers relying on quasi-static approximations of the Maxwell's system are usually employed to address the low-frequency regime. In particular, the simulation of eddy currents (i.e., conductive currents generated by a time-varying magnetic field [13], [14]), of great interest for many industrial applications [15], has historically required the use of quasi-static solvers that neglect displacement currents [16]. One of the most severe drawback related to these approximations is the challenge of handling the simulation of multiscale scenarios which restricts their use in real case, complex apparatuses.

Several preconditioning techniques based on the Calderón identities have been proposed for the PMCHWT formulation, relying on the fact that the PMCHWT operator, when properly discretized, is a valid preconditioner for itself [11], [17], [18]. While immune from the dense-discretization breakdown, these formulations still suffer from contrast dependent instabilities [11] and undesired current cancellations at very low frequency, which dramatically affect the accuracy of the simulation outcomes [12], [19]. An appropriate rescaling of the quasi-Helmholtz decomposed solenoidal and quasi-irrotational components of the system has been proven effective in addressing this issue [10]. However, when the quasi-Helmholtz decomposition is performed by means of the loop-star change of basis, the condition number behavior with respect to the

Received 29 October 2024; revised 23 February 2025; accepted 26 March 2025. Date of publication 14 April 2025; date of current version 6 August 2025. This work was supported in part by the European Innovation Council (EIC) through the European Union's Horizon Europe Research Programme under Grant 101046748 (Project CEREBRO); and in part by the European Union-Next Generation EU within the Piano Nazionale di Ripresa e Resilienza (PNRR) Project "Multiscale Modeling and Engineering Applications" of the Italian National Center for High Performance Computing (HPC), Big Data and Quantum Computing (Spoke 6)-PNRR M4C2, Investimento 1.4-Avviso n. 3138 del 16/12/2021-CN00000013 National Centre for HPC, Big Data and Quantum Computing (HPC) under Grant CUP E13C22000990001. *(Corresponding author: Francesco P. Andriulli.)*

Viviana Giunzioni, Alberto Scazzola, and Francesco P. Andriulli are with the Department of Electronics and Telecommunications, Politecnico di Torino, 10129 Turin, Italy (e-mail: francesco.andriulli@polito.it).

Adrien Merlini is with the Microwave Department, IMT Atlantique, 29238 Brest, France (e-mail: adrien.merlini@imt-atlantique.fr).

Digital Object Identifier 10.1109/TAP.2025.3558603

mesh refinement is even worsened [10]. Also, the computationally costly explicit detection of the global-loop quasi-harmonic subspace is required. This typically requires the search for the holes and handles of the geometries or the evaluation of the nullspace of the loop-star transformation matrix [10], which can degrade the computational complexity of the overall problem that ideally should equal that of solving well-conditioned integral equations accelerated with fast solvers [20].

Alternatively, the quasi-Helmholtz components of the system can be retrieved by projection, that is, by multiplication of the operator matrix with the quasi-Helmholtz projectors, introduced in [20] and [21] and proved effective at curing the PMCHWT equation's low frequency breakdown in [19]. Their use brings along two significant advantages with respect to the standard loop-star decomposition, which are: 1) the quasi-harmonic subspace is included in the solenoidal subspace spanned by the solenoidal projector, so that the global-loops detection is not required and 2) the use of the quasi-Helmholtz projector does not affect the behavior of the condition number with respect to discretization [10].

Using this tool, we develop here a new preconditioning strategy capable of stabilizing the PMCHWT equation with respect to the physical parameters of the problem in the whole low-frequency regime, including the eddy-current one [13], and, contextually, preventing detrimental current cancellations in presence of both inductive and capacitive type magnetic frill excitations. Built upon the standard PMCHWT equation, our full-wave formulation allows for seamless transitions between low and high frequencies, as well as between dielectric and conductive scatterers, resulting in a versatile and computationally efficient solver, compatible with state-of-the-art acceleration strategies [22], [23].

The article is organized as follows. After setting the necessary background and notation in Section II, Sections III and IV aim at analyzing the shortcomings of the PMCHWT formulation. In particular, Section III, presents an analysis of the asymptotic scalings of the quasi-Helmholtz components of the system as a function of frequency and of the conductivity of the scattering body. Section IV, is focused on the dominant component analysis of the equivalent currents induced by a voltage generator modeled as a magnetic frill, which is a common type of excitation employed in circuit simulation. Then, in Section V, we define a quasi-Helmholtz projectors-based preconditioning strategy and determine the multiplicative coefficients used in the rescaling of the quasi-Helmholtz components of the system, allowing for the stabilization of the PMCHWT equation with respect to both the electrical length and the conductivity of the scatterer and for the correct recovery of the currents dominant components. The numerical results in Section VI aim at illustrating the good conditioning properties of the proposed formulation applied to both simply and multiply connected geometries, with respect to both frequency and conductivity and the accuracy of the results. Finally, concluding remarks will be given in Section VII.

II. Background and Notation

Let $\Omega_1 \subset \mathbb{R}^3$ be a closed, bounded conductive region with boundary $\Gamma = \partial\Omega_1$ characterized by the outward pointing normal $\hat{\boldsymbol{n}}$, surrounded by the complementary vacuum region $\Omega_0 = \mathbb{R}^3 \backslash \bar{\Omega}_1$, with permittivity ϵ_0 and permeability μ_0. The domain Ω_1, of characteristic length L, is filled with a linear, homogeneous, and isotropic conductive medium of permeability $\mu_1 = \mu_r\mu_0$ and complex permittivity $\epsilon_1 = \epsilon_r'\epsilon_0 - j\sigma/\omega$, where σ is the conductivity, and ω is the angular frequency.

Given a wavenumber k and the 3-D free-space Green's function associated with it [4], $G_k(\boldsymbol{r},\boldsymbol{r}') := \mathrm{e}^{-\mathrm{j}kR}/(4\pi R)$, with $R := \|\boldsymbol{r}-\boldsymbol{r}'\|$, the electric field integral operator (EFIO) and magnetic field integral operator (MFIO), $\mathcal{T}_k$ and $\mathcal{K}_k$, are defined as [3] and [4]

$$\left(\mathcal{T}_k \boldsymbol{f}\right)(\boldsymbol{r}) := -\mathrm{j}k\left(\mathcal{T}_{A,k}\boldsymbol{f}\right)(\boldsymbol{r}) + \frac{1}{\mathrm{j}k}\left(\mathcal{T}_{\Phi,k}\boldsymbol{f}\right)(\boldsymbol{r}) \tag{1}$$

$$\left(\mathcal{K}_k \boldsymbol{f}\right)(\boldsymbol{r}) := \hat{\boldsymbol{n}} \times \text{p.v.} \int_\Gamma \nabla G_k\left(\boldsymbol{r},\boldsymbol{r}'\right) \times \boldsymbol{f}\left(\boldsymbol{r}'\right) \mathrm{d}\boldsymbol{r}' \tag{2}$$

$$\left(\mathcal{T}_{A,k}\boldsymbol{f}\right)(\boldsymbol{r}) := \hat{\boldsymbol{n}} \times \int_\Gamma G_k\left(\boldsymbol{r},\boldsymbol{r}'\right)\boldsymbol{f}\left(\boldsymbol{r}'\right)\mathrm{d}\boldsymbol{r}' \tag{3}$$

$$\left(\mathcal{T}_{\Phi,k}\boldsymbol{f}\right)(\boldsymbol{r}) := \hat{\boldsymbol{n}} \times \nabla \int_\Gamma G_k\left(\boldsymbol{r},\boldsymbol{r}'\right)\nabla' \cdot \boldsymbol{f}\left(\boldsymbol{r}'\right)\mathrm{d}\boldsymbol{r}' \tag{4}$$

where p.v. indicates Cauchy principal value. When an incident electromagnetic field $(\boldsymbol{E}^i, \boldsymbol{H}^i)$ impinges on Ω_1, the resulting electric and magnetic surface current densities $\boldsymbol{j}_s := \hat{\boldsymbol{n}} \times \boldsymbol{H}$ and $\boldsymbol{m}_s := -\hat{\boldsymbol{n}} \times \boldsymbol{E}$ satisfy the PMCHWT equation [5],

$$\begin{pmatrix} \eta_0\mathcal{T}_{k_0} + \eta_1\mathcal{T}_{k_1} & -\left(\mathcal{K}_{k_0} + \mathcal{K}_{k_1}\right) \\ \left(\mathcal{K}_{k_0} + \mathcal{K}_{k_1}\right) & \frac{1}{\eta_0}\mathcal{T}_{k_0} + \frac{1}{\eta_1}\mathcal{T}_{k_1} \end{pmatrix} \begin{pmatrix} \boldsymbol{j}_s \\ \boldsymbol{m}_s \end{pmatrix} = \begin{pmatrix} -\hat{\boldsymbol{n}} \times \boldsymbol{E}^i \\ -\hat{\boldsymbol{n}} \times \boldsymbol{H}^i \end{pmatrix} \tag{5}$$

where $k_{0,1} := \omega\sqrt{\epsilon_{0,1}\mu_{0,1}}$ is the wavenumber in $\Omega_{0,1}$ and $\eta_{0,1} := \sqrt{\mu_{0,1}/\epsilon_{0,1}}$ is the characteristic impedance of the exterior or interior medium. In the evaluation of the above square roots, the branch is chosen in accordance with the definition of propagative and lossy Green's functions, compatibly with the convention $e^{-\mathrm{j}kR}$.

To discretize and numerically solve (5), we approximate the surface Γ with a mesh of planar triangular elements with average edge length h, over which we can define different sets of basis functions. In the following, we will consider Rao–Wilton–Glisson (RWG) basis functions. For their definition and visual representation, we refer to [10] and references therein. By expanding the unknown current densities as linear combinations of RWG functions, as

$$\boldsymbol{j}_s = \sum_{n=1}^{N_e} j_n \boldsymbol{f}_n, \quad \boldsymbol{m}_s = \sum_{n=1}^{N_e} m_n \boldsymbol{f}_n \tag{6}$$

where N_e is the number of edges in the mesh, and by testing the resulting equations with curl-conforming rotated RWG functions, following a conforming Petrov–Galerkin discretization procedure, we obtain the linear system of equations:

$$\begin{pmatrix} \boldsymbol{T}_u & -\boldsymbol{K} \\ \boldsymbol{K} & \boldsymbol{T}_l \end{pmatrix} \begin{pmatrix} \boldsymbol{j} \\ \boldsymbol{m} \end{pmatrix} = \begin{pmatrix} \boldsymbol{e} \\ \boldsymbol{h} \end{pmatrix}, \qquad \begin{pmatrix} \boldsymbol{T}_u & -\boldsymbol{K} \\ \boldsymbol{K} & \boldsymbol{T}_l \end{pmatrix} =: \boldsymbol{Z} \tag{7}$$

where

$$\boldsymbol{K} := \boldsymbol{K}_{k_0} + \boldsymbol{K}_{k_1} \tag{8}$$

$$\boldsymbol{T}_u := \eta_0 \boldsymbol{T}_{k_0} + \eta_1 \boldsymbol{T}_{k_1} \tag{9}$$

$$\boldsymbol{T}_l := \frac{1}{\eta_0}\boldsymbol{T}_{k_0} + \frac{1}{\eta_1}\boldsymbol{T}_{k_1}. \tag{10}$$

The elements of the above matrices discretizing the EFIO and MFIO read

$$(\boldsymbol{T}_k)_{mn} \coloneqq -\mathrm{j}k\left(\boldsymbol{T}_{A,k}\right)_{mn} + \frac{1}{\mathrm{j}k}\left(\boldsymbol{T}_{\Phi,k}\right)_{mn} \tag{11}$$

$$(\boldsymbol{K}_k)_{mn} \coloneqq \left(\hat{\boldsymbol{n}} \times \boldsymbol{f}_m, \mathcal{K}_k\left(\boldsymbol{f}_n\right)\right)_{L^2(\Gamma)} \tag{12}$$

$$\left(\boldsymbol{T}_{A,k}\right)_{mn} \coloneqq \left(\hat{\boldsymbol{n}} \times \boldsymbol{f}_m, \mathcal{T}_{A,k}\left(\boldsymbol{f}_n\right)\right)_{L^2(\Gamma)} \tag{13}$$

$$\left(\boldsymbol{T}_{\Phi,k}\right)_{mn} \coloneqq \left(\hat{\boldsymbol{n}} \times \boldsymbol{f}_m, \mathcal{T}_{\Phi,k}\left(\boldsymbol{f}_n\right)\right)_{L^2(\Gamma)}. \tag{14}$$

The right-hand-side (RHS) resulting from the testing procedure is

$$(\boldsymbol{e})_m \coloneqq \left(\hat{\boldsymbol{n}} \times \boldsymbol{f}_m, -\hat{\boldsymbol{n}} \times \boldsymbol{E}^i\right)_{L^2(\Gamma)} \tag{15}$$

$$(\boldsymbol{h})_m \coloneqq \left(\hat{\boldsymbol{n}} \times \boldsymbol{f}_m, -\hat{\boldsymbol{n}} \times \boldsymbol{H}^i\right)_{L^2(\Gamma)} \tag{16}$$

while the elements of the unknown vector are simply given by $(\boldsymbol{j})_n \coloneqq j_n$ and $(\boldsymbol{m})_n \coloneqq m_n$. In the following we will focus on a rescaled version of the equation, that is, on matrix $\bar{Z}$, which reads:

$$\underbrace{\begin{pmatrix} \boldsymbol{T}_u/\eta_0 & -\boldsymbol{K} \\ \boldsymbol{K} & \eta_0 \boldsymbol{T}_l \end{pmatrix}}_{\bar{Z}} \begin{pmatrix} \sqrt{\eta_0}\boldsymbol{j} \\ \boldsymbol{m}/\sqrt{\eta_0} \end{pmatrix} = \begin{pmatrix} \boldsymbol{e}/\sqrt{\eta_0} \\ \sqrt{\eta_0}\boldsymbol{h} \end{pmatrix} \tag{17}$$

where

$$\boldsymbol{T}_u/\eta_0 = \boldsymbol{T}_{k_0} - \mathrm{j}k_0\mu_r \boldsymbol{T}_{A,k_1} + \frac{1}{\mathrm{j}k_0\epsilon_r}\boldsymbol{T}_{\Phi,k_1} \tag{18}$$

$$\eta_0 \boldsymbol{T}_l = \boldsymbol{T}_{k_0} - \mathrm{j}k_0\epsilon_r \boldsymbol{T}_{A,k_1} + \frac{1}{\mathrm{j}k_0\mu_r}\boldsymbol{T}_{\Phi,k_1}. \tag{19}$$

This rescaling leads to an effective conductivity stabilization at mid-frequencies, as will be shown in the following, but cannot prevent the dramatic increase of the conditioning toward lower frequencies.

We introduce at this point the mixed Gram matrices $\boldsymbol{G}$ and $\mathbb{G} = -\boldsymbol{G}^{\mathrm{T}}$, defined as $(\boldsymbol{G})_{mn} \coloneqq (\hat{\boldsymbol{n}} \times \boldsymbol{f}_m, \boldsymbol{g}_n)_{L^2(\Gamma)}$ and $(\mathbb{G})_{mn} \coloneqq (\hat{\boldsymbol{n}} \times \boldsymbol{g}_m, \boldsymbol{f}_n)_{L^2(\Gamma)}$, where g_n is the dual with respect to the RWG function defined on the nth edge. In this work, we employed Buffa–Christiansen (BC) functions but other possibilities are feasible (see [10] and references therein for the definition of BC functions and for further details).

In Section III, we will apply the loop-star decomposition technique to the PMCHWT operator for analyzing its spectral properties, and we denote with Λ, $\boldsymbol{H}$, and Σ the transformation matrices from the loop, global loop, and star subspaces to the RWG subspace. For their explicit definition and interpretation, we refer the reader to [10] and [21]. We also define the block matrix $\boldsymbol{A}$ as $\boldsymbol{A} \coloneqq (\Sigma \quad \boldsymbol{H} \quad \Sigma)$, that can be used to perform the required decomposition. It is worth noting that we are only introducing matrix $\boldsymbol{H}$ for the purpose of the analysis, but its explicit (potentially costly) evaluation will not be required for the implementation of the proposed formulation. The main building blocks of the actual preconditioning scheme presented in this work are the quasi-Helmholtz projectors, for both primal and dual spaces, defined as

$$\boldsymbol{P}^{\Sigma} \coloneqq \Sigma\left(\Sigma^{\mathrm{T}}\Sigma\right)^{+}\Sigma^{\mathrm{T}}, \qquad \boldsymbol{P}^{\Lambda\boldsymbol{H}} \coloneqq \boldsymbol{I} - \boldsymbol{P}^{\Sigma} \tag{20}$$

$$\mathbb{P}^{\Lambda} \coloneqq \Lambda\left(\Lambda^{\mathrm{T}}\Lambda\right)^{+}\Lambda^{\mathrm{T}}, \qquad \mathbb{P}^{\Sigma\boldsymbol{H}} \coloneqq \boldsymbol{I} - \mathbb{P}^{\Lambda} \tag{21}$$

where the subscript $^{+}$ indicates the Moore–Penrose pseudoinvserse. In particular, $\boldsymbol{P}^{\Sigma}$ and $\mathbb{P}^{\Lambda}$ are the nonsolenoidal projectors for primal and dual functions, built, respectively, from the star and the loop transformation matrices, given that the dual BC functions represent a rotation of the primal RWG functions; by complementarity, $\boldsymbol{P}^{\Lambda\boldsymbol{H}}$ and $\mathbb{P}^{\Sigma\boldsymbol{H}}$ are the solenoidal projectors for primal and dual functions, that means that they are projectors onto the solenoidal subspace—which includes the quasi-harmonic subspace. Taking advantage of algebraic multigrid preconditioning techniques, these projectors can be applied to a vector in quasi-linear complexity [10], characteristic which makes them compatible with standard fast solvers.

III. Conditioning Analysis of the PMCHWT Equation

This section aims at studying some of the spectral properties of the PMCHWT system matrix $\bar{Z}$ in the low-frequency regime and for different conductivity levels σ of the body Ω. The analysis is based on the determination of the asymptotic scalings toward low frequency of the quasi-Helmholtz components of the decomposed system, where the decomposition is performed by means of loop and star transformation matrices, for analytical purposes only.

First, after recalling that $L = \mathrm{diam}(\Omega_1)$, we introduce the dimensionless scalar parameters

$$\chi \coloneqq k_0 L \tag{22}$$

$$\gamma \coloneqq \sqrt{\omega\epsilon_0/\sigma} \tag{23}$$

$$\xi \coloneqq \sqrt{2/\mu_r}L/\delta \tag{24}$$

where δ denotes the skin depth parameter, or penetration length of the field inside the scatterer, which is function of the frequency and the conductivity and defined as $\delta \coloneqq \sqrt{2/(\omega\sigma\mu_1)}$. Given the definitions above, we have $\chi = \gamma\xi$. Before moving to the study of the interior Green's function kernel, strictly dependent on the frequency-conductivity regime considered (the nomenclature of which has been partially borrowed from [2]), we start by analyzing the asymptotic behavior of matrices $\boldsymbol{T}_{A,k_0}$, $\boldsymbol{T}_{\Phi,k_0}$, and $\boldsymbol{K}_{k_0}$ for vanishing frequency, as well as their loop-star components. In the low-frequency limit, for $\chi \to 0$, the exterior Green's function and its gradient can be expanded as

$$G_{k_0}\left(\boldsymbol{r},\boldsymbol{r}'\right) = \frac{1}{4\pi R}\left[1 - \mathrm{j}\frac{R}{L}\chi - \frac{R^2}{2L^2}\chi^2 + \mathcal{O}\left(\chi^3\right)\right] \tag{25}$$

$$\nabla G_{k_0}\left(\boldsymbol{r},\boldsymbol{r}'\right) = \frac{1}{4\pi}\left[\nabla\left(\frac{1}{R}\right) - \frac{\chi^2}{2L^2}\nabla R + \mathcal{O}\left(\chi^3\right)\right]. \tag{26}$$

From these expansions, it can be recognized that, for $\chi \to 0$

$$\|\boldsymbol{T}_{A,k_0}/L\| = \mathcal{O}(1), \quad \|\boldsymbol{K}_{k_0}\| = \mathcal{O}(1) \tag{27}$$

$$\|\boldsymbol{T}_{\Phi,k_0}L\| = \mathcal{O}(1), \quad \|\boldsymbol{K}_{\mathrm{ext},k_0}\| = \mathcal{O}\left(\chi^2\right) \tag{28}$$

where $\boldsymbol{K}_{\mathrm{ext},k} = \boldsymbol{K}_k - \boldsymbol{K}_0$. Here and in the following, the notation $f = \mathcal{O}(g)$ indicates that there exists $c > 0$ such that $|f| \leq c|g|$ in the indicated limit. Note that in this contribution, we consider the low-frequency limit and thus the constant c may be function of the mesh refinement parameter h, that is, $c = c(h)$. However, this characterization of c in function of h is

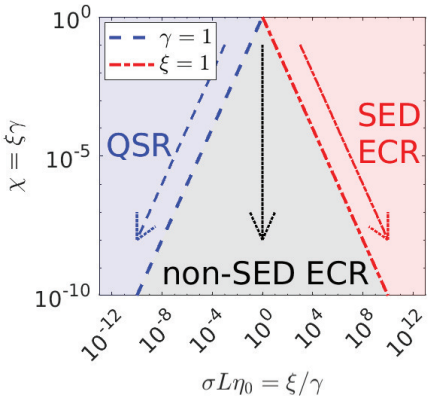

Fig. 1. Graphical representation of the low-frequency limits in the three regions: the blue arrow represents the limit direction in the QSR, the black arrow in the non-SED ECR, and the red arrow in the SED ECR.

outside the scope of this work. Equations (27) and (28) result in the loop-star decompositions

$$\boldsymbol{A}^{\mathrm{T}}\left(\boldsymbol{T}_{k_0}\right)\boldsymbol{A} = \mathcal{O}\begin{pmatrix}\chi & \chi & \chi\\ \chi & \chi & \chi\\ \chi & \chi & \chi^{-1}\end{pmatrix} \tag{29}$$

$$\boldsymbol{A}^{\mathrm{T}}\left(\boldsymbol{K}_{k_0}\right)\boldsymbol{A} = \mathcal{O}\begin{pmatrix}\chi^2 & \chi^2 & 1\\ \chi^2 & 1 & 1\\ 1 & 1 & 1\end{pmatrix} \tag{30}$$

where we have enforced the cancellation of the scalar potential contribution when tested against or applied to a solenoidal function [20]

$$\Lambda^{\mathrm{T}}\boldsymbol{T}_{\Phi,k} = \boldsymbol{0}\,, \quad \boldsymbol{H}^{\mathrm{T}}\boldsymbol{T}_{\Phi,k} = \boldsymbol{0}\,, \quad \boldsymbol{T}_{\Phi,k}\Lambda = \boldsymbol{0}\,, \quad \boldsymbol{T}_{\Phi,k}\boldsymbol{H} = \boldsymbol{0} \tag{31}$$

and the cancellation of the static magnetic field operator $\boldsymbol{K}_0$ [24]

$$\Lambda^{\mathrm{T}}\boldsymbol{K}_0\Lambda = \boldsymbol{0}\,, \quad \Lambda^{\mathrm{T}}\boldsymbol{K}_0\boldsymbol{H} = \boldsymbol{0}\,, \quad \boldsymbol{H}^{\mathrm{T}}\boldsymbol{K}_0\Lambda = \boldsymbol{0}\,. \tag{32}$$

The decompositions in (30) will be useful to determine the overall loop-star decomposed PMCHWT matrix $\boldsymbol{Z}_{\Lambda\boldsymbol{H}\Sigma}$

$$\boldsymbol{Z}_{\Lambda\boldsymbol{H}\Sigma} \coloneqq \begin{pmatrix}\boldsymbol{A}^{\mathrm{T}} & \boldsymbol{0}\\ \boldsymbol{0} & \boldsymbol{A}^{\mathrm{T}}\end{pmatrix}\bar{Z}\begin{pmatrix}\boldsymbol{A} & \boldsymbol{0}\\ \boldsymbol{0} & \boldsymbol{A}\end{pmatrix}. \tag{33}$$

We proceed now to the definition of the three low-frequency regimes considered in this work and to the interior kernel analysis.

A. Analysis in the QSR

The quasi-static region is characterized by slowly varying fields, for which the quasi-stationary condition $\chi \ll 1$ holds true. In addition, the ratio between the angular frequency and the conductivity should be high enough to make any conductive current inside the object negligible with respect to the displacement current induced by the impinging field. In formulae, the quasi-static region is characterized by

$$\begin{cases}\chi \ll 1\\ \gamma \gg 1\end{cases} \tag{34}$$

The asymptotic behavior of the blocks of the loop-star decomposed PMCHWT equation, allowing the study of the stability properties of the formulation, can be deduced from the low-frequency asymptotic expansion of the interior Green's function and of its gradient, under the assumption $\gamma \gg 1$. This corresponds to analyzing the low-frequency limit along a constant$-\gamma$ line (blue arrow in Fig. 1, corresponding to $\sigma \propto \omega$) with $\gamma \gg 1$. The regime characterized by $\gamma = \text{const} \gg 1$ while $\chi \to 0$ will be referred to as quasi-static regime (QSR).

Along this limit, both the real and the imaginary part of the interior wavenumber go to zero. In particular, writing the expression of the interior wavenumber in the form

$$k_1 = k_0\sqrt{\epsilon_r'\mu_r}\sqrt{1 - \mathrm{j}\frac{\sigma}{\omega\epsilon_0\epsilon_r'}} \tag{35}$$

shows that, for $\chi \to 0$, $\Re\{k_1 L\} = \mathcal{O}(\chi)$ and $\Im\{k_1 L\} = \mathcal{O}(\chi)/\gamma^2$. This fact allows us to exploit the small argument Taylor expansions of the Green's function and of its gradient to determine the low-frequency scalings

$$\|\boldsymbol{T}_{A,k_1}/L\| = \mathcal{O}(1)\,, \quad \|\boldsymbol{K}_{k_1}\| = \mathcal{O}(1) \tag{36}$$

$$\|\boldsymbol{T}_{\Phi,k_1}L\| = \mathcal{O}(1)\,, \quad \|\boldsymbol{K}_{\mathrm{ext},k_1}\| = \mathcal{O}\left(\chi^2\right) \tag{37}$$

leading to the quasi-Helmholtz decomposition

$$\boldsymbol{Z}_{\Lambda\boldsymbol{H}\Sigma} = \mathcal{O}\begin{pmatrix}\chi & \chi & \chi & \chi^2 & \chi^2 & 1\\ \chi & \chi & \chi & \chi^2 & 1 & 1\\ \chi & \chi & \chi^{-1} & 1 & 1 & 1\\ \chi^2 & \chi^2 & 1 & \chi & \chi & \chi\\ \chi^2 & 1 & 1 & \chi & \chi & \chi\\ 1 & 1 & 1 & \chi & \chi & \chi^{-1}\end{pmatrix}. \tag{38}$$

By applying the Gershgorin circle theorem, we recognize that the condition number of the PMCHWT equation grows when decreasing the frequency, resulting in the so-called low-frequency breakdown of the formulation. Moreover, we infer that, as in the EFIE case [20], the pathological frequency behavior of the condition number is in part due to the opposed frequency scaling of the vector and scalar potential components of the electric operator $\mathcal{T}_k$. Numerical evidence indicates that the condition number of the PMCHWT formulation increases as ω^{-2} in the low-frequency limit, as for the EFIE.

B. Analysis in the Non-SED ECR

The eddy-current region is a quasi-stationary region ($\chi \ll 1$) in which the typical time-scale is longer than the electric relaxation time constant $\tau = \epsilon_0/\sigma$, i.e., $\omega\tau \ll 1$, equivalent to $\gamma \ll 1$. In addition, the nonskin-effect-dominated subset of the eddy-current region is characterized by a further condition on the skin depth parameter, which should be much larger with respect to the characteristic size of the object, resulting in the condition $\xi \ll 1$ in the regime under study. Therefore, in the nonskin-effect-dominated eddy-current region, the frequency, geometrical, and electrical parameters of the scatterer are such that

$$\begin{cases}\chi \ll 1\\ \gamma \ll 1\\ \xi \ll 1.\end{cases} \tag{39}$$

In the eddy-current region ($\chi \ll 1$ and $\gamma \ll 1$), the interior wavenumber, which after some manipulations can be written as

$$k_1 = \frac{1-\mathrm{j}}{\delta}\sqrt{1+\mathrm{j}\frac{\omega\epsilon_0\epsilon_r'}{\sigma}} \tag{40}$$

can be approximated as $k_1 \simeq (1-\mathrm{j})/\delta$. Hence, both the real and the imaginary parts of $k_1 L$ decrease in magnitude as ξ when decreasing the frequency.

In this region, we want to analyze the low-frequency limit of the PMCHWT equation by keeping the ratio ξ/γ constant (i.e., constant conductivity), corresponding to the black arrow in Fig. 1. This regime, characterized by $\xi/\gamma = \text{const}$ while $\chi \to 0$, will be referred to as nonskin-effect-dominated eddy-current regime (non-SED ECR). Along this limit, $\Re\{k_1 L\} = \mathcal{O}(\chi/\gamma)$ and $\Im\{k_1 L\} = \mathcal{O}(\chi/\gamma)$ for $\chi \to 0$. Once again, we can take advantage of the small argument expansions of the Green's function and of its gradient to determine the scalings

$$\|\boldsymbol{T}_{A,k_1}/L\| = \mathcal{O}(1)\,, \quad \|\boldsymbol{K}_{k_1}\| = \mathcal{O}(1) \tag{41}$$

$$\|\boldsymbol{T}_{\Phi,k_1} L\| = \mathcal{O}(1)\,, \quad \|\boldsymbol{K}_{\mathrm{ext},k_1}\| = \mathcal{O}(\chi/\gamma)^2\,. \tag{42}$$

The loop-star decomposed PMCHWT equation in the non-SED ECR limit follows as:

$$\boldsymbol{Z}_{\Lambda\boldsymbol{H}\Sigma} = \mathcal{O}\begin{pmatrix} \chi & \chi & \chi & \chi^2\gamma^{-2} & \chi^2\gamma^{-2} & 1 \\ \chi & \chi & \chi & \chi^2\gamma^{-2} & 1 & 1 \\ \chi & \chi & \chi^{-1} & 1 & 1 & 1 \\ \chi^2\gamma^{-2} & \chi^2\gamma^{-2} & 1 & \chi\gamma^{-2} & \chi\gamma^{-2} & \chi\gamma^{-2} \\ \chi^2\gamma^{-2} & 1 & 1 & \chi\gamma^{-2} & \chi\gamma^{-2} & \chi\gamma^{-2} \\ 1 & 1 & 1 & \chi\gamma^{-2} & \chi\gamma^{-2} & \chi^{-1} \end{pmatrix}. \tag{43}$$

As in the previous case, the application of the Gershgorin circle theorem shows a low-frequency breakdown of the equation, as the condition number grows at least as ω^{-1} in the low-frequency limit.

Indeed, the matrix eigenvalues lie in three Gershgorin circles with radius $\mathcal{O}(1)$ and centered in values which are $\mathcal{O}(\chi)$, $\mathcal{O}(\chi^{-1})$, and $\mathcal{O}(\chi\gamma^{-2})$. Also notice that, when fixing the frequency, $\chi\gamma^{-2} = \sigma\eta_0 L$ ranges from χ to χ^{-1} when the conductivity varies from $\sigma_{\mathrm{low}} \coloneqq \omega\epsilon_0$ (corresponding to $\gamma = 1$) to $\sigma_{\mathrm{high}} \coloneqq (\omega L^2\mu_1)^{-1}$ (corresponding to $\xi = 1$).

C. Analysis in the SED ECR

The skin-effect-dominated eddy-current region is characterized by

$$\begin{cases} \chi \ll 1 \\ \gamma \ll 1 \\ \xi \gg 1. \end{cases} \tag{44}$$

In this case, we aim at studying the asymptotic behavior of the equation in the low-frequency limit along a constant–ξ line, with $\xi \gg 1$ (red arrow in Fig. 1, corresponding to $\sigma \propto \omega^{-1}$). This regime, characterized by $\xi = \text{const} \gg 1$ while $\chi \to 0$, will be referred to as skin-effect-dominated eddy-current regime (SED ECR).

The eddy-current conditions ($\chi \ll 1$ and $\gamma \ll 1$) guarantee the validity of the approximation of the interior wavenumber as $k_1 \simeq (1-\mathrm{j})/\delta$ mentioned before. The fundamental difference with respect to the other low-frequency regimes analyzed above is that in this case the product $k_1 L$ does not vanish in the low-frequency limit, preventing the use of the Maclaurin series of the Green's function and its gradient for the evaluation of the asymptotic behavior of the operators. However, by noting that the Green's function behavior is dominated by the exponential decay $\mathrm{e}^{-R/\delta}$, through some technical steps, it can be proved that

$$\|\boldsymbol{T}_{A,k_1}/L\| = \xi^{-1}\mathcal{O}(1)\,, \quad \|\boldsymbol{K}_{k_1}\| = \xi^{-1}\mathcal{O}(1)\,, \tag{45}$$

$$\|\boldsymbol{T}_{\Phi,k_1} L\| = \xi^{-1}\mathcal{O}(1)\,, \quad \|\boldsymbol{K}_{\mathrm{ext},k_1}\| = \mathcal{O}(1) \tag{46}$$

for $\chi \to 0$, where $\xi^{-1} = \gamma/\chi$ is constant.

Indeed, as far as the vector and scalar electric potentials are concerned, it can be seen that, in the low-skin-depth limit, only the self and near interactions give rise to a nonnegligible contribution as the skin depth becomes smaller than the characteristic size of the mesh triangles h. Hence, we can grasp an intuition of the above scalings by noting that the Green's function kernel in modulo can be approximated as $|G_k(\boldsymbol{r},\boldsymbol{r}')| \simeq \mathrm{e}^{-R/\delta}/(4\pi R)$ and that the integral of such function over an infinite plane, which is a good estimate of the integral over the triangle T due to the exponential decay of the function for source points inside T and testing points outside T, is

$$\int_{\mathbb{R}^2} \frac{\mathrm{e}^{-|\boldsymbol{r}|/\delta}}{4\pi|\boldsymbol{r}|}\mathrm{d}\boldsymbol{r} = \delta/2 \tag{47}$$

determining the scalings of the norms $\|\boldsymbol{T}_{A,k_1}\|$ and $\|\boldsymbol{T}_{\Phi,k_1}\|$ with the skin depth. Also, in the same low-skin-depth-limit, the MFIO matrix becomes negligible, as the kernel exactly cancels for testing points lying on the source triangle. Finally, each of $\boldsymbol{T}_{A,k_1}$, $\boldsymbol{T}_{\Phi,k_1}$, and $\boldsymbol{K}_{k_1}$, denoted here with the placeholder $\boldsymbol{M}$, can be written as the sum of a matrix accounting for the interactions between basis functions defined on nonoverlapping domains, $\boldsymbol{M}_{\mathrm{far}}$, and the remaining $\boldsymbol{M}_{\mathrm{near}}$, that is $\boldsymbol{M} = \boldsymbol{M}_{\mathrm{near}} + \boldsymbol{M}_{\mathrm{far}}$. It can be shown that, in the low-frequency limit, $\|\boldsymbol{M}_{\mathrm{far}}\| = e^{-p\xi}\mathcal{O}(1)$, where $pL > 0$ represents the minimum distance between two nonoverlapping domains of basis functions. Hence, $\|\boldsymbol{M}\| \le \|\boldsymbol{M}_{\mathrm{near}}\| + \|\boldsymbol{M}_{\mathrm{far}}\| = \xi^{-1}\mathcal{O}(1) + e^{-p\xi}\mathcal{O}(1)$.

The accurate evaluation of the inner integrals for the definition of the operator matrices is not trivial and may require the implementation of different integration techniques specifically tailored to highly lossy media. In our work, we employed the integration scheme presented in [25] to produce accurate numerical results.

Due to the condition $\gamma \ll 1$ the diagonal blocks of $\bar{Z}$ can be approximated as

$$\boldsymbol{T}_u/\eta_0 \simeq \boldsymbol{T}_{k_0} - \mathrm{j}k_0\mu_r\boldsymbol{T}_{A,k_1} + \frac{1}{\sigma\eta_0 L}\left(\boldsymbol{T}_{\Phi,k_1} L\right) \tag{48}$$

$$\boldsymbol{T}_l \cdot \eta_0 \simeq \boldsymbol{T}_{k_0} - \sigma\eta_0 L\left(\boldsymbol{T}_{A,k_1}/L\right) + \frac{1}{\mathrm{j}k_0\mu_r}\boldsymbol{T}_{\Phi,k_1}\,. \tag{49}$$

It holds $\sigma\eta_0 L = \chi\gamma^{-2} \gg \chi^{-1}$ (following from the condition $\xi \gg 1$). As a result, in the SED ECR, the asymptotic behavior of the upper diagonal block is determined by $\boldsymbol{T}_{k_0}$, while the behavior of the lower diagonal block is determined by the dominating term $\sigma\eta_0 L(\boldsymbol{T}_{A,k_1}/L)$, for which it holds

$$\|\sigma\eta_0 L\left(\boldsymbol{T}_{A,k_1}/L\right)\| = \mathcal{O}\left(\chi\gamma^{-2}\xi^{-1}\right) = \mathcal{O}\left(\gamma^{-1}\right)\,. \tag{50}$$

Under these conditions, the loop-star decomposition of the PMCHWT equation in the SED ECR is

$$\boldsymbol{Z}_{\Lambda\boldsymbol{H}\Sigma} = \mathcal{O}\begin{pmatrix} \chi & \chi & \chi & 1 & 1 & 1 \\ \chi & \chi & \chi & 1 & 1 & 1 \\ \chi & \chi & \chi^{-1} & 1 & 1 & 1 \\ 1 & 1 & 1 & \gamma^{-1} & \gamma^{-1} & \gamma^{-1} \\ 1 & 1 & 1 & \gamma^{-1} & \gamma^{-1} & \gamma^{-1} \\ 1 & 1 & 1 & \gamma^{-1} & \gamma^{-1} & \gamma^{-1} \end{pmatrix}. \tag{51}$$

Also, in this regime, the formulation is plagued by the low-frequency breakdown, that is, the condition number of $\bar{Z}$ increases at least as ω^{-1} in the low-frequency limit. Moreover, a further instability with respect to σ can be recognized in the high-conductivity limit, related to the branch of singular values accumulating at $\mathcal{O}(\gamma^{-1})$, with γ^{-1} always higher that χ^{-1} in the SED ECR, resulting in a condition number increase when fixing the frequency and increasing the conductivity of the scatterer.

Before moving to the definition of a quasi-Helmholtz projectors-based preconditioning strategy capable of curing the instabilities identified so far, we first propose an asymptotic analysis of the quasi-Helmholtz components of the solution of the system, allowing to determine the current contributions required for the accurate evaluation of the electric and magnetic fields inside and outside the scatterer in the low-frequency limit. This preliminary analysis will indeed result in further requirements to be satisfied in the design of the preconditioning strategy.

IV. Asymptotic Analysis of the Current Components

While a stable and low matrix condition number is required for the convergence of an iterative solver [26], it is not sufficient to guarantee the accuracy of the solution [10], [19], [20]. Indeed, numerical loss of significance at low frequencies can provoke the corruption of some nondominant quasi-Helmholtz current components, which, in turn, can lower the accuracy of the scattered fields. In this section, we present a low-frequency asymptotic analysis aimed at determining which are the current components required for the correct reconstruction of the electric and magnetic fields inside and outside the body Ω. This information will constitute a further constraint in the design of the preconditioning strategy, which will have to allow for the correct recovery of these required current components.

The analysis will take advantage of the low-frequency asymptotic expansion of the PMCHWT equation along the low-frequency limits previously identified, which are, along a constant$-\gamma$ line with $\gamma \gg 1$ for the QSR, along a constant$-(\xi/\gamma)$ line with $\xi \gg 1$ and $\gamma \gg 1$ for the non-SED ECR, and along a constant$-\xi$ line with $\xi \gg 1$ for the SED ECR. These three limits are graphically represented as arrows in Fig. 1.

We aim at determining the asymptotic scalings of the loop, star, and quasi-harmonic components of the system, both in their real and imaginary parts, along these limits. For the sake of simplicity, the ω dependency will be explicitly extracted, that is, the limits will be expressed in terms of $\omega \to 0$.

By following the same reasoning as above, after evaluating the low-frequency asymptotic behavior of the interior and exterior wavenumber, resulting in the operator scalings in real and imaginary parts, we can estimate the asymptotic scalings of the quasi-Helmholtz decomposed blocks of the PMCHWT equation by enforcing the proper cancellations [(31) and (32)].

In addition, notice that the imaginary part of $\boldsymbol{T}_{A,k}$ may present a different scaling depending on whether the source or test basis function is solenoidal or nonsolenoidal. Indeed, in the case of solenoidal basis functions, the second term in the Green's function Maclaurin expansion vanishes.

Then, from the above mentioned decomposition, the asymptotic scalings of the quasi-Helmholtz decomposed inverse matrix $\boldsymbol{Z}^{-1}_{\Lambda\boldsymbol{H}\Sigma}$ can be retrieved, for example by applying the Woodbury formula [27] or by leveraging symbolic calculations. Numerical validation can further ensure the correctness of the low-frequency asymptotic behavior of the quasi-Helmholtz components of the system retrieved from this analysis. These results are summarized in the following.

A. Quasi-Static Regime

As already shown in Section III-A, the interior wavenumber asymptotic behavior in the QSR is $\Re\{k_1 L\} = \mathcal{O}(\omega)$, $\Im\{k_1 L\} = \mathcal{O}(\omega)$. This results in the loop-star decomposition of matrix $\bar{Z}$ in the low-frequency limit as

$$\Re\{\boldsymbol{Z}_{\Lambda\boldsymbol{H}\Sigma}\} = \mathcal{O}\begin{pmatrix} \omega^3 & \omega^3 & \omega^3 & \omega^2 & \omega^2 & 1 \\ \omega^3 & \omega^3 & \omega^3 & \omega^2 & 1 & 1 \\ \omega^3 & \omega^3 & \omega^{-1} & 1 & 1 & 1 \\ \omega^2 & \omega^2 & 1 & \omega & \omega & \omega \\ \omega^2 & 1 & 1 & \omega & \omega & \omega \\ 1 & 1 & 1 & \omega & \omega & 1 \end{pmatrix} \tag{52}$$

$$\Im\{\boldsymbol{Z}_{\Lambda\boldsymbol{H}\Sigma}\} = \mathcal{O}\begin{pmatrix} \omega & \omega & \omega & \omega^2 & \omega^2 & \omega^2 \\ \omega & \omega & \omega & \omega^2 & \omega^2 & \omega^2 \\ \omega & \omega & \omega^{-1} & \omega^2 & \omega^2 & \omega^2 \\ \omega^2 & \omega^2 & \omega^2 & \omega & \omega & \omega \\ \omega^2 & \omega^2 & \omega^2 & \omega & \omega & \omega \\ \omega^2 & \omega^2 & \omega^2 & \omega & \omega & \omega^{-1} \end{pmatrix}. \tag{53}$$

The loop-star decomposition of the matrix inverse behaves as

$$\Re\{\boldsymbol{Z}^{-1}_{\Lambda\boldsymbol{H}\Sigma}\} = \mathcal{O}\begin{pmatrix} 1 & \omega & \omega & 1 & 1 & 1 \\ \omega & \omega & \omega & 1 & 1 & \omega^2 \\ \omega & \omega & \omega & 1 & \omega^2 & \omega^2 \\ 1 & 1 & 1 & \omega^{-1} & \omega & \omega \\ 1 & 1 & \omega^2 & \omega & \omega^2 & \omega^2 \\ 1 & \omega^2 & \omega^2 & \omega & \omega^2 & \omega^2 \end{pmatrix} \tag{54}$$

$$\Im\{\boldsymbol{Z}^{-1}_{\Lambda\boldsymbol{H}\Sigma}\} = \mathcal{O}\begin{pmatrix} \omega^{-1} & \omega & \omega & 1 & \omega & \omega \\ \omega & \omega & \omega & 1 & \omega^2 & \omega^2 \\ \omega & \omega & \omega & 1 & \omega^2 & \omega^2 \\ 1 & 1 & 1 & \omega^{-1} & \omega & \omega \\ \omega & \omega^2 & \omega^2 & \omega & \omega & \omega \\ \omega & \omega^2 & \omega^2 & \omega & \omega & \omega \end{pmatrix}. \tag{55}$$

B. Nonskin-Effect-Dominated Eddy-Current Regime

The low-frequency asymptotic behavior of the interior wavenumber in the non-SED ECR is $\Re\{k_1 L\} = \mathcal{O}(\omega^{1/2})$, $\Im\{k_1 L\} = \mathcal{O}(\omega^{1/2})$ for $\omega \to 0$. This results in the following

asymptotic behavior of the loop-star decomposed system and its inverse

$$\Re\{\boldsymbol{Z}_{\Lambda H\Sigma}\} = \mathcal{O}\begin{pmatrix} \omega^2 & \omega^2 & \omega^2 & \omega^{3/2} & \omega^{3/2} & 1 \\ \omega^2 & \omega^2 & \omega^2 & \omega^{3/2} & 1 & 1 \\ \omega^2 & \omega^2 & 1 & 1 & 1 & 1 \\ \omega^{3/2} & \omega^{3/2} & 1 & 1 & 1 & 1 \\ \omega^{3/2} & 1 & 1 & 1 & 1 & 1 \\ 1 & 1 & 1 & 1 & 1 & \omega^{-1/2} \end{pmatrix} \tag{56}$$

$$\Im\{\boldsymbol{Z}_{\Lambda H\Sigma}\} = \mathcal{O}\begin{pmatrix} \omega & \omega & \omega & \omega & \omega & \omega \\ \omega & \omega & \omega & \omega & \omega & \omega \\ \omega & \omega & \omega^{-1} & \omega & \omega & \omega \\ \omega & \omega & \omega & \omega & \omega & \omega \\ \omega & \omega & \omega & \omega & \omega & \omega \\ \omega & \omega & \omega & \omega & \omega & \omega^{-1} \end{pmatrix} \tag{57}$$

and

$$\Re\{\boldsymbol{Z}^{-1}_{\Lambda H\Sigma}\} = \mathcal{O}\begin{pmatrix} \omega^{-1/2} & 1 & \omega^{3/2} & 1 & 1 & 1 \\ 1 & 1 & \omega^2 & 1 & 1 & \omega^{3/2} \\ \omega^{3/2} & \omega^2 & \omega^2 & \omega^2 & \omega^2 & \omega^2 \\ 1 & 1 & \omega^2 & 1 & \omega^{3/2} & \omega^{3/2} \\ 1 & 1 & \omega^2 & \omega^{3/2} & \omega^{3/2} & \omega^{3/2} \\ 1 & \omega^{3/2} & \omega^2 & \omega^{3/2} & \omega^{3/2} & \omega^{3/2} \end{pmatrix} \tag{58}$$

$$\Im\{\boldsymbol{Z}^{-1}_{\Lambda H\Sigma}\} = \mathcal{O}\begin{pmatrix} \omega^{-1} & \omega^{1/2} & \omega & \omega^{1/2} & \omega^{1/2} & \omega^{1/2} \\ \omega^{1/2} & \omega & \omega & \omega & \omega & \omega \\ \omega & \omega & \omega & \omega & \omega^{5/2} & \omega^{5/2} \\ \omega^{1/2} & \omega & \omega & \omega & \omega & \omega \\ \omega^{1/2} & \omega & \omega^{5/2} & \omega & \omega & \omega \\ \omega^{1/2} & \omega & \omega^{5/2} & \omega & \omega & \omega \end{pmatrix}. \tag{59}$$

C. Skin-Effect-Dominated Eddy-Current Regime

The product $(k_1 L)$ stays constant in the low-frequency limit considered in this case, that is, $\Re\{k_1 L\} = \mathcal{O}(1)$, $\Im\{k_1 L\} = \mathcal{O}(1)$ for $\omega \to 0$. The loop-star decomposition of matrix $\bar{Z}$ then behaves as

$$\Re\{\boldsymbol{Z}_{\Lambda H\Sigma}\} = \mathcal{O}\begin{pmatrix} \omega & \omega & \omega & 1 & 1 & 1 \\ \omega & \omega & \omega & 1 & 1 & 1 \\ \omega & \omega & 1 & 1 & 1 & 1 \\ 1 & 1 & 1 & \omega^{-1} & \omega^{-1} & \omega^{-1} \\ 1 & 1 & 1 & \omega^{-1} & \omega^{-1} & \omega^{-1} \\ 1 & 1 & 1 & \omega^{-1} & \omega^{-1} & \omega^{-1} \end{pmatrix} \tag{60}$$

$$\Im\{\boldsymbol{Z}_{\Lambda H\Sigma}\} = \mathcal{O}\begin{pmatrix} \omega & \omega & \omega & 1 & 1 & 1 \\ \omega & \omega & \omega & 1 & 1 & 1 \\ \omega & \omega & \omega^{-1} & 1 & 1 & 1 \\ 1 & 1 & 1 & \omega^{-1} & \omega^{-1} & \omega^{-1} \\ 1 & 1 & 1 & \omega^{-1} & \omega^{-1} & \omega^{-1} \\ 1 & 1 & 1 & \omega^{-1} & \omega^{-1} & \omega^{-1} \end{pmatrix}. \tag{61}$$

The loop-star decomposition of the matrix inverse is

$$\Re\{\boldsymbol{Z}^{-1}_{\Lambda H\Sigma}\} = \mathcal{O}\begin{pmatrix} \omega^{-1} & \omega^{-1} & \omega & 1 & 1 & 1 \\ \omega^{-1} & \omega^{-1} & \omega & 1 & 1 & 1 \\ \omega & \omega & \omega^2 & \omega^2 & \omega^2 & \omega^2 \\ 1 & 1 & \omega^2 & \omega & \omega & \omega \\ 1 & 1 & \omega^2 & \omega & \omega & \omega \\ 1 & 1 & \omega^2 & \omega & \omega & \omega \end{pmatrix} \tag{62}$$

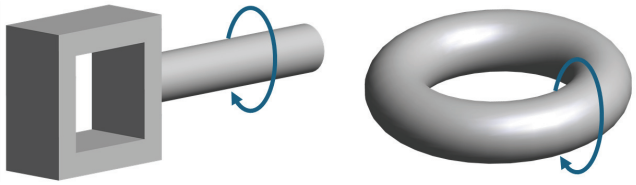

Fig. 2. Magnetic frill excitation, represented as a blue arrow, is inductive (right) if there is a global loop of the geometry passing through the frill, capacitive (left) otherwise.

$$\Im\{\boldsymbol{Z}^{-1}_{\Lambda H\Sigma}\} = \mathcal{O}\begin{pmatrix} \omega^{-1} & \omega^{-1} & \omega & 1 & 1 & 1 \\ \omega^{-1} & \omega^{-1} & \omega & 1 & 1 & 1 \\ \omega & \omega & \omega & \omega^2 & \omega^2 & \omega^2 \\ 1 & 1 & \omega^2 & \omega & \omega & \omega \\ 1 & 1 & \omega^2 & \omega & \omega & \omega \\ 1 & 1 & \omega^2 & \omega & \omega & \omega \end{pmatrix}. \tag{63}$$

D. Excitation Definition and Resulting Solution

The behavior of the different components of the excitation vector are required to determine the behavior of the components of the solution of the PMCHWT.

In this work, we focus on the magnetic frill excitation [28], [29], as it is one of the most common ways to model an imposed potential difference in the circuital framework that allows for a closed form expression of the impressed electric and magnetic fields (differently from other excitation types, such as the voltage gap).

The low-frequency asymptotic scalings of the quasi-Helmholtz components of the electric and magnetic fields produced by a magnetic frill have already been studied in [19] and are reported in the following tables. It is worth noting that, following the reasoning in [24], the harmonic component of the electric field shows a different behavior depending on whether there exists a global loop of the geometry passing through the magnetic frill or not, resulting in an inductive excitation or a capacitive one, respectively (see Fig. 2), both of which will be studied in the following.

By applying the inverse of the operator matrices to the resulting RHSs, it is possible to retrieve the low-frequency asymptotic scalings of the quasi-Helmholtz components of the surface current densities and, from them, to identify the dominant components, i.e., the components that are dominant in the low-frequency limits considered. The scattering of each of the current components, in their real and imaginary parts, results in a component of the electromagnetic fields. As a result of this analysis, the current components required to correctly reconstruct the fields in the three regimes for the two types of excitations considered are summarized in Tables I and II, in the right column of sections (c), (d), (e), and (f).

When solving numerically the standard PMCHWT in floating point arithmetic, the real parts (or imaginary parts) of the loop and star components of the currents are stored in the same floating point number. In the low-frequency limit, this determines a loss of information about the nondominant current components, lying outside the dynamic range of the

TABLE I

SCALINGS OF THE REAL AND IMAGINARY PARTS OF QUANTITIES OF INTEREST WHEN $\omega \to 0$ FOR AN INDUCTIVE MAGNETIC FRILL EXCITATION

(a) Right hand side							
Excitation	$(\Re,\Im)(\boldsymbol{E}^i_{\boldsymbol{\Lambda}})$	$(\Re,\Im)(\boldsymbol{E}^i_{\boldsymbol{H}})$	$(\Re,\Im)(\boldsymbol{E}^i_{\boldsymbol{\Sigma}})$	$(\Re,\Im)(\boldsymbol{H}^i_{\boldsymbol{\Lambda}})$	$(\Re,\Im)(\boldsymbol{H}^i_{\boldsymbol{H}})$	$(\Re,\Im)(\boldsymbol{H}^i_{\boldsymbol{\Sigma}})$	
Inductive	$(\omega^2,\,\omega^3)$	$(1,\,\omega^3)$	$(1,\,\omega^3)$	$(\omega^4,\,\omega)$	$(\omega^4,\,\omega)$	$(\omega^4,\,\omega)$	
(b) Surface current density							
Regime	$(\Re,\Im)(\boldsymbol{j}_{\boldsymbol{\Lambda}})$	$(\Re,\Im)(\boldsymbol{j}_{\boldsymbol{H}})$	$(\Re,\Im)(\boldsymbol{j}_{\boldsymbol{\Sigma}})$	$(\Re,\Im)(\boldsymbol{m}_{\boldsymbol{\Lambda}})$	$(\Re,\Im)(\boldsymbol{m}_{\boldsymbol{H}})$	$(\Re,\Im)(\boldsymbol{m}_{\boldsymbol{\Sigma}})$	Current dominant components
QSR	$(\omega,\,\omega)$	$(\omega,\,\omega)$	$(\omega,\,\omega)$	$(1,\,1)$	$(1,\,\omega^2)$	$(\omega^2,\,\omega^2)$	$\Re(\boldsymbol{j}_{\boldsymbol{\Lambda}},\boldsymbol{j}_{\boldsymbol{H}},\boldsymbol{j}_{\boldsymbol{\Sigma}},\boldsymbol{m}_{\boldsymbol{\Lambda}},\boldsymbol{m}_{\boldsymbol{H}})$ $\Im(\boldsymbol{j}_{\boldsymbol{\Lambda}},\boldsymbol{j}_{\boldsymbol{H}},\boldsymbol{j}_{\boldsymbol{\Sigma}},\boldsymbol{m}_{\boldsymbol{\Lambda}})$
non-SED ECR	$(1,\,\omega^{1/2})$	$(1,\,\omega)$	$(\omega^2,\,\omega)$	$(1,\,\omega)$	$(1,\,\omega)$	$(\omega^{3/2},\,\omega)$	$\Re(\boldsymbol{j}_{\boldsymbol{\Lambda}},\boldsymbol{j}_{\boldsymbol{H}},\boldsymbol{m}_{\boldsymbol{\Lambda}},\boldsymbol{m}_{\boldsymbol{H}})$ $\Im(\boldsymbol{j}_{\boldsymbol{\Lambda}},\boldsymbol{m}_{\boldsymbol{\Lambda}},\boldsymbol{m}_{\boldsymbol{H}},\boldsymbol{m}_{\boldsymbol{\Sigma}})$
SED ECR	$(\omega^{-1},\,\omega^{-1})$	$(\omega^{-1},\,\omega^{-1})$	$(\omega,\,\omega)$	$(1,\,1)$	$(1,\,1)$	$(1,\,1)$	$\Re(\boldsymbol{j}_{\boldsymbol{\Lambda}},\boldsymbol{j}_{\boldsymbol{H}},\boldsymbol{m}_{\boldsymbol{\Lambda}},\boldsymbol{m}_{\boldsymbol{H}},\boldsymbol{m}_{\boldsymbol{\Sigma}})$ $\Im(\boldsymbol{j}_{\boldsymbol{\Lambda}},\boldsymbol{j}_{\boldsymbol{H}},\boldsymbol{m}_{\boldsymbol{\Lambda}},\boldsymbol{m}_{\boldsymbol{H}},\boldsymbol{m}_{\boldsymbol{\Sigma}})$
(c) Electric interior near field							
Regime	$\boldsymbol{E}(\Re\boldsymbol{j}_{\boldsymbol{\Lambda}})$ $\boldsymbol{E}(\Im\boldsymbol{j}_{\boldsymbol{\Lambda}})$	$\boldsymbol{E}(\Re\boldsymbol{j}_{\boldsymbol{H}})$ $\boldsymbol{E}(\Im\boldsymbol{j}_{\boldsymbol{H}})$	$\boldsymbol{E}(\Re\boldsymbol{j}_{\boldsymbol{\Sigma}})$ $\boldsymbol{E}(\Im\boldsymbol{j}_{\boldsymbol{\Sigma}})$	$\boldsymbol{E}(\Re\boldsymbol{m}_{\boldsymbol{\Lambda}})$ $\boldsymbol{E}(\Im\boldsymbol{m}_{\boldsymbol{\Lambda}})$	$\boldsymbol{E}(\Re\boldsymbol{m}_{\boldsymbol{H}})$ $\boldsymbol{E}(\Im\boldsymbol{m}_{\boldsymbol{H}})$	$\boldsymbol{E}(\Re\boldsymbol{m}_{\boldsymbol{\Sigma}})$ $\boldsymbol{E}(\Im\boldsymbol{m}_{\boldsymbol{\Sigma}})$	Current dominant components
QSR	$(\omega^4,\,\omega^2)$ $(\omega^2,\,\omega^4)$	$(\omega^4,\,\omega^2)$ $(\omega^2,\,\omega^4)$	$(1,\,1)$ $(1,\,1)$	$(1,\,\omega^2)$ $(\omega^2,\,1)$	$(1,\,\omega^2)$ $(\omega^4,\,\omega^2)$	$(\omega^2,\,\omega^4)$ $(\omega^4,\,\omega^2)$	$\Re(\boldsymbol{j}_{\boldsymbol{\Sigma}},\boldsymbol{m}_{\boldsymbol{\Lambda}},\boldsymbol{m}_{\boldsymbol{H}})$ $\Im(\boldsymbol{j}_{\boldsymbol{\Sigma}},\boldsymbol{m}_{\boldsymbol{\Lambda}})$
non-SED ECR	$(\omega^2,\,\omega)$ $(\omega^{3/2},\,\omega^{5/2})$	$(\omega^2,\,\omega)$ $(\omega^2,\,\omega^3)$	$(\omega^2,\,\omega^3)$ $(\omega^2,\,\omega)$	$(1,\,\omega)$ $(\omega^2,\,\omega)$	$(1,\,\omega)$ $(\omega^2,\,\omega)$	$(\omega^{3/2},\,\omega^{5/2})$ $(\omega^2,\,\omega)$	$\Re(\boldsymbol{m}_{\boldsymbol{\Lambda}},\boldsymbol{m}_{\boldsymbol{H}})$
SED ECR	$(1,\,1)$ $(1,\,1)$	$(1,\,1)$ $(1,\,1)$	$(\omega^2,\,\omega^2)$ $(\omega^2,\,\omega^2)$	$(1,\,1)$ $(1,\,1)$	$(1,\,1)$ $(1,\,1)$	$(1,\,1)$ $(1,\,1)$	$\Re(\boldsymbol{j}_{\boldsymbol{\Lambda}},\boldsymbol{j}_{\boldsymbol{H}},\boldsymbol{m}_{\boldsymbol{\Lambda}},\boldsymbol{m}_{\boldsymbol{H}},\boldsymbol{m}_{\boldsymbol{\Sigma}})$ $\Im(\boldsymbol{j}_{\boldsymbol{\Lambda}},\boldsymbol{j}_{\boldsymbol{H}},\boldsymbol{m}_{\boldsymbol{\Lambda}},\boldsymbol{m}_{\boldsymbol{H}},\boldsymbol{m}_{\boldsymbol{\Sigma}})$
(d) Magnetic interior near field							
Regime	$\boldsymbol{H}(\Re\boldsymbol{j}_{\boldsymbol{\Lambda}})$ $\boldsymbol{H}(\Im\boldsymbol{j}_{\boldsymbol{\Lambda}})$	$\boldsymbol{H}(\Re\boldsymbol{j}_{\boldsymbol{H}})$ $\boldsymbol{H}(\Im\boldsymbol{j}_{\boldsymbol{H}})$	$\boldsymbol{H}(\Re\boldsymbol{j}_{\boldsymbol{\Sigma}})$ $\boldsymbol{H}(\Im\boldsymbol{j}_{\boldsymbol{\Sigma}})$	$\boldsymbol{H}(\Re\boldsymbol{m}_{\boldsymbol{\Lambda}})$ $\boldsymbol{H}(\Im\boldsymbol{m}_{\boldsymbol{\Lambda}})$	$\boldsymbol{H}(\Re\boldsymbol{m}_{\boldsymbol{H}})$ $\boldsymbol{H}(\Im\boldsymbol{m}_{\boldsymbol{H}})$	$\boldsymbol{H}(\Re\boldsymbol{m}_{\boldsymbol{\Sigma}})$ $\boldsymbol{H}(\Im\boldsymbol{m}_{\boldsymbol{\Sigma}})$	Current dominant components
QSR	$(\omega,\,\omega^3)$ $(\omega^3,\,\omega)$	$(\omega,\,\omega^3)$ $(\omega^3,\,\omega)$	$(\omega,\,\omega^3)$ $(\omega^3,\,\omega)$	$(\omega,\,\omega)$ $(\omega,\,\omega)$	$(\omega,\,\omega)$ $(\omega^3,\,\omega^3)$	$(\omega^3,\,\omega)$ $(\omega,\,\omega^3)$	$\Re(\boldsymbol{j}_{\boldsymbol{\Lambda}},\boldsymbol{j}_{\boldsymbol{H}},\boldsymbol{j}_{\boldsymbol{\Sigma}},\boldsymbol{m}_{\boldsymbol{\Lambda}},\boldsymbol{m}_{\boldsymbol{H}},\boldsymbol{m}_{\boldsymbol{\Sigma}})$ $\Im(\boldsymbol{j}_{\boldsymbol{\Lambda}},\boldsymbol{j}_{\boldsymbol{H}},\boldsymbol{j}_{\boldsymbol{\Sigma}},\boldsymbol{m}_{\boldsymbol{\Lambda}},\boldsymbol{m}_{\boldsymbol{\Sigma}})$
non-SED ECR	$(1,\,\omega)$ $(\omega^{3/2},\,\omega^{1/2})$	$(1,\,\omega)$ $(\omega^2,\,\omega)$	$(\omega^2,\,\omega^3)$ $(\omega^2,\,\omega)$	$(1,\,\omega)$ $(\omega^2,\,\omega)$	$(1,\,\omega)$ $(\omega^2,\,\omega)$	$(\omega^{3/2},\,\omega^{1/2})$ $(1,\,\omega)$	$\Re(\boldsymbol{j}_{\boldsymbol{\Lambda}},\boldsymbol{j}_{\boldsymbol{H}},\boldsymbol{m}_{\boldsymbol{\Lambda}},\boldsymbol{m}_{\boldsymbol{H}})$ $\Im(\boldsymbol{m}_{\boldsymbol{\Sigma}})$
SED ECR	$(\omega^{-1},\,\omega^{-1})$ $(\omega^{-1},\,\omega^{-1})$	$(\omega^{-1},\,\omega^{-1})$ $(\omega^{-1},\,\omega^{-1})$	$(\omega,\,\omega)$ $(\omega,\,\omega)$	$(\omega^{-1},\,\omega^{-1})$ $(\omega^{-1},\,\omega^{-1})$	$(\omega^{-1},\,\omega^{-1})$ $(\omega^{-1},\,\omega^{-1})$	$(\omega^{-1},\,\omega^{-1})$ $(\omega^{-1},\,\omega^{-1})$	$\Re(\boldsymbol{j}_{\boldsymbol{\Lambda}},\boldsymbol{j}_{\boldsymbol{H}},\boldsymbol{m}_{\boldsymbol{\Lambda}},\boldsymbol{m}_{\boldsymbol{H}},\boldsymbol{m}_{\boldsymbol{\Sigma}})$ $\Im(\boldsymbol{j}_{\boldsymbol{\Lambda}},\boldsymbol{j}_{\boldsymbol{H}},\boldsymbol{m}_{\boldsymbol{\Lambda}},\boldsymbol{m}_{\boldsymbol{H}},\boldsymbol{m}_{\boldsymbol{\Sigma}})$
(e) Electric exterior near field							
Regime	$\boldsymbol{E}(\Re\boldsymbol{j}_{\boldsymbol{\Lambda}})$ $\boldsymbol{E}(\Im\boldsymbol{j}_{\boldsymbol{\Lambda}})$	$\boldsymbol{E}(\Re\boldsymbol{j}_{\boldsymbol{H}})$ $\boldsymbol{E}(\Im\boldsymbol{j}_{\boldsymbol{H}})$	$\boldsymbol{E}(\Re\boldsymbol{j}_{\boldsymbol{\Sigma}})$ $\boldsymbol{E}(\Im\boldsymbol{j}_{\boldsymbol{\Sigma}})$	$\boldsymbol{E}(\Re\boldsymbol{m}_{\boldsymbol{\Lambda}})$ $\boldsymbol{E}(\Im\boldsymbol{m}_{\boldsymbol{\Lambda}})$	$\boldsymbol{E}(\Re\boldsymbol{m}_{\boldsymbol{H}})$ $\boldsymbol{E}(\Im\boldsymbol{m}_{\boldsymbol{H}})$	$\boldsymbol{E}(\Re\boldsymbol{m}_{\boldsymbol{\Sigma}})$ $\boldsymbol{E}(\Im\boldsymbol{m}_{\boldsymbol{\Sigma}})$	Current dominant components
QSR	$(\omega^5,\,\omega^2)$ $(\omega^2,\,\omega^5)$	$(\omega^5,\,\omega^2)$ $(\omega^2,\,\omega^5)$	$(\omega^3,\,1)$ $(1,\,\omega^3)$	$(1,\,\omega^3)$ $(\omega^3,\,1)$	$(1,\,\omega^3)$ $(\omega^5,\,\omega^2)$	$(\omega^2,\,\omega^5)$ $(\omega^5,\,\omega^2)$	$\Re(\boldsymbol{j}_{\boldsymbol{\Sigma}},\boldsymbol{m}_{\boldsymbol{\Lambda}},\boldsymbol{m}_{\boldsymbol{H}})$ $\Im(\boldsymbol{j}_{\boldsymbol{\Sigma}},\boldsymbol{m}_{\boldsymbol{\Lambda}})$
non-SED ECR	$(\omega^4,\,\omega)$ $(\omega^{3/2},\,\omega^{9/2})$	$(\omega^4,\,\omega)$ $(\omega^2,\,\omega^5)$	$(\omega^4,\,\omega)$ $(1,\,\omega^3)$	$(1,\,\omega^3)$ $(\omega^4,\,\omega)$	$(1,\,\omega^3)$ $(\omega^4,\,\omega)$	$(\omega^{3/2},\,\omega^{9/2})$ $(\omega^4,\,\omega)$	$\Re(\boldsymbol{m}_{\boldsymbol{\Lambda}},\boldsymbol{m}_{\boldsymbol{H}})$ $\Im(\boldsymbol{j}_{\boldsymbol{\Sigma}})$
SED ECR	$(\omega^3,\,1)$ $(1,\,\omega^3)$	$(\omega^3,\,1)$ $(1,\,\omega^3)$	$(\omega^3,\,1)$ $(1,\,\omega^3)$	$(1,\,\omega^3)$ $(\omega^3,\,1)$	$(1,\,\omega^3)$ $(\omega^3,\,1)$	$(1,\,\omega^3)$ $(\omega^3,\,1)$	$\Re(\boldsymbol{j}_{\boldsymbol{\Lambda}},\boldsymbol{j}_{\boldsymbol{H}},\boldsymbol{j}_{\boldsymbol{\Sigma}},\boldsymbol{m}_{\boldsymbol{\Lambda}},\boldsymbol{m}_{\boldsymbol{H}},\boldsymbol{m}_{\boldsymbol{\Sigma}})$ $\Im(\boldsymbol{j}_{\boldsymbol{\Lambda}},\boldsymbol{j}_{\boldsymbol{H}},\boldsymbol{j}_{\boldsymbol{\Sigma}},\boldsymbol{m}_{\boldsymbol{\Lambda}},\boldsymbol{m}_{\boldsymbol{H}},\boldsymbol{m}_{\boldsymbol{\Sigma}})$
(f) Magnetic exterior near field							
Regime	$\boldsymbol{H}(\Re\boldsymbol{j}_{\boldsymbol{\Lambda}})$ $\boldsymbol{H}(\Im\boldsymbol{j}_{\boldsymbol{\Lambda}})$	$\boldsymbol{H}(\Re\boldsymbol{j}_{\boldsymbol{H}})$ $\boldsymbol{H}(\Im\boldsymbol{j}_{\boldsymbol{H}})$	$\boldsymbol{H}(\Re\boldsymbol{j}_{\boldsymbol{\Sigma}})$ $\boldsymbol{H}(\Im\boldsymbol{j}_{\boldsymbol{\Sigma}})$	$\boldsymbol{H}(\Re\boldsymbol{m}_{\boldsymbol{\Lambda}})$ $\boldsymbol{H}(\Im\boldsymbol{m}_{\boldsymbol{\Lambda}})$	$\boldsymbol{H}(\Re\boldsymbol{m}_{\boldsymbol{H}})$ $\boldsymbol{H}(\Im\boldsymbol{m}_{\boldsymbol{H}})$	$\boldsymbol{H}(\Re\boldsymbol{m}_{\boldsymbol{\Sigma}})$ $\boldsymbol{H}(\Im\boldsymbol{m}_{\boldsymbol{\Sigma}})$	Current dominant components
QSR	$(\omega,\,\omega^4)$ $(\omega^4,\,\omega)$	$(\omega,\,\omega^4)$ $(\omega^4,\,\omega)$	$(\omega,\,\omega^4)$ $(\omega^4,\,\omega)$	$(\omega^4,\,\omega)$ $(\omega,\,\omega^4)$	$(\omega^4,\,\omega)$ $(\omega^3,\,\omega^6)$	$(\omega^4,\,\omega)$ $(\omega,\,\omega^4)$	$\Re(\boldsymbol{j}_{\boldsymbol{\Lambda}},\boldsymbol{j}_{\boldsymbol{H}},\boldsymbol{j}_{\boldsymbol{\Sigma}},\boldsymbol{m}_{\boldsymbol{\Lambda}},\boldsymbol{m}_{\boldsymbol{H}},\boldsymbol{m}_{\boldsymbol{\Sigma}})$ $\Im(\boldsymbol{j}_{\boldsymbol{\Lambda}},\boldsymbol{j}_{\boldsymbol{H}},\boldsymbol{j}_{\boldsymbol{\Sigma}},\boldsymbol{m}_{\boldsymbol{\Lambda}},\boldsymbol{m}_{\boldsymbol{\Sigma}})$
non-SED ECR	$(1,\,\omega^3)$ $(\omega^{7/2},\,\omega^{1/2})$	$(1,\,\omega^3)$ $(\omega^4,\,\omega)$	$(\omega^2,\,\omega^5)$ $(\omega^4,\,\omega)$	$(\omega^4,\,\omega)$ $(\omega^2,\,\omega^5)$	$(\omega^4,\,\omega)$ $(\omega^2,\,\omega^5)$	$(\omega^{7/2},\,\omega^{1/2})$ $(1,\,\omega^3)$	$\Re(\boldsymbol{j}_{\boldsymbol{\Lambda}},\boldsymbol{j}_{\boldsymbol{H}})$ $\Im(\boldsymbol{m}_{\boldsymbol{\Sigma}})$
SED ECR	$(\omega^{-1},\,\omega^2)$ $(\omega^2,\,\omega^{-1})$	$(\omega^{-1},\,\omega^2)$ $(\omega^2,\,\omega^{-1})$	$(\omega,\,\omega^4)$ $(\omega^4,\,\omega)$	$(\omega^4,\,\omega)$ $(\omega,\,\omega^4)$	$(\omega^4,\,\omega)$ $(\omega,\,\omega^4)$	$(\omega^2,\,\omega^{-1})$ $(\omega^{-1},\,\omega^2)$	$\Re(\boldsymbol{j}_{\boldsymbol{\Lambda}},\boldsymbol{j}_{\boldsymbol{H}},\boldsymbol{m}_{\boldsymbol{\Sigma}})$ $\Im(\boldsymbol{j}_{\boldsymbol{\Lambda}},\boldsymbol{j}_{\boldsymbol{H}},\boldsymbol{m}_{\boldsymbol{\Sigma}})$
(g) Rescaled current density							
Regime	$a_R^{-1}\boldsymbol{j}_{\boldsymbol{\Lambda}}$	$a_R^{-1}\boldsymbol{j}_{\boldsymbol{H}}$	$b_R^{-1}\boldsymbol{j}_{\boldsymbol{\Sigma}}$	$c_R^{-1}\boldsymbol{m}_{\boldsymbol{\Lambda}}$	$c_R^{-1}\boldsymbol{m}_{\boldsymbol{H}}$	$d_R^{-1}\boldsymbol{m}_{\boldsymbol{\Sigma}}$	Recovered components
QSR	$(1,1)$	$(1,1)$	$(1,1)$	$(1,1)$	$(1,\omega^2)$	$(1,1)$	$\Re(\boldsymbol{j}_{\boldsymbol{\Lambda}},\boldsymbol{j}_{\boldsymbol{H}},\boldsymbol{j}_{\boldsymbol{\Sigma}},\boldsymbol{m}_{\boldsymbol{\Lambda}},\boldsymbol{m}_{\boldsymbol{H}},\boldsymbol{m}_{\boldsymbol{\Sigma}})$ $\Im(\boldsymbol{j}_{\boldsymbol{\Lambda}},\boldsymbol{j}_{\boldsymbol{H}},\boldsymbol{j}_{\boldsymbol{\Sigma}},\boldsymbol{m}_{\boldsymbol{\Lambda}},\boldsymbol{m}_{\boldsymbol{\Sigma}})$
non-SED ECR	$(\omega^{1/2},\omega)$	$(\omega^{1/2},\omega^{3/2})$	$(\omega,1)$	$(1,\omega)$	$(1,\omega)$	$(\omega,\omega^{1/2})$	$\Re(\boldsymbol{j}_{\boldsymbol{\Lambda}},\boldsymbol{j}_{\boldsymbol{H}},\boldsymbol{m}_{\boldsymbol{\Lambda}},\boldsymbol{m}_{\boldsymbol{H}})$ $\Im(\boldsymbol{j}_{\boldsymbol{\Sigma}},\boldsymbol{m}_{\boldsymbol{\Sigma}})$
SED ECR	$(\omega^{-1/2},\omega^{-1/2})$	$(\omega^{-1/2},\omega^{-1/2})$	$(\omega^{-1/2},\omega^{-1/2})$	$(\omega^{-1/2},\omega^{-1/2})$	$(\omega^{-1/2},\omega^{-1/2})$	$(\omega^{-1/2},\omega^{-1/2})$	$\Re(\boldsymbol{j}_{\boldsymbol{\Lambda}},\boldsymbol{j}_{\boldsymbol{H}},\boldsymbol{j}_{\boldsymbol{\Sigma}},\boldsymbol{m}_{\boldsymbol{\Lambda}},\boldsymbol{m}_{\boldsymbol{H}},\boldsymbol{m}_{\boldsymbol{\Sigma}})$ $\Im(\boldsymbol{j}_{\boldsymbol{\Lambda}},\boldsymbol{j}_{\boldsymbol{H}},\boldsymbol{j}_{\boldsymbol{\Sigma}},\boldsymbol{m}_{\boldsymbol{\Lambda}},\boldsymbol{m}_{\boldsymbol{H}},\boldsymbol{m}_{\boldsymbol{\Sigma}})$

floating point number determined by the larger current contributions. Nevertheless, the lost components may be crucial in the reconstruction of the fields. Indeed, by comparing the current components required for the correct evaluation of the scattered fields with the ones that can be retrieved without proper rescaling of the quasi-Helmholtz components of the system in the right column of section (b), one can notice that in many cases the current resulting from a naive solution of the PMCHWT equation does not allow for the correct reconstruction of the fields. For example, from Table I we infer that, in the non-SED ECR, the current component $\Im(\boldsymbol{j}_{\boldsymbol{\Sigma}})$ is required for a correct reconstruction of the exterior electric field; however, this component is lost in numerical cancellation in the low-frequency limit if a proper rescaling of the current coefficients is not applied, resulting in a deterioration of the accuracy of the scattered field.

Now that the critical components of the current have been identified, we can design our preconditioning strategy with the objective of preserving them in addition to curing the ill-conditioning of the matrix.

TABLE II

SCALINGS OF THE REAL AND IMAGINARY PARTS OF QUANTITIES OF INTEREST WHEN $\omega \to 0$ FOR A CAPACITIVE MAGNETIC FRILL EXCITATION

(a) Right hand side							
Excitation	$(\Re,\Im)(\boldsymbol{E}^i_{\Lambda})$	$(\Re,\Im)(\boldsymbol{E}^i_{H})$	$(\Re,\Im)(\boldsymbol{E}^i_{\Sigma})$	$(\Re,\Im)(\boldsymbol{H}^i_{\Lambda})$	$(\Re,\Im)(\boldsymbol{H}^i_{H})$	$(\Re,\Im)(\boldsymbol{H}^i_{\Sigma})$	
Capacitive	$(\omega^2,\,\omega^3)$	$(\omega^2,\,\omega^3)$	$(1,\,\omega^3)$	$(\omega^4,\,\omega)$	$(\omega^4,\,\omega)$	$(\omega^4,\,\omega)$	
(b) Surface current density							
Regime	$(\Re,\Im)(\boldsymbol{j}_{\Lambda})$	$(\Re,\Im)(\boldsymbol{j}_{H})$	$(\Re,\Im)(\boldsymbol{j}_{\Sigma})$	$(\Re,\Im)(\boldsymbol{m}_{\Lambda})$	$(\Re,\Im)(\boldsymbol{m}_{H})$	$(\Re,\Im)(\boldsymbol{m}_{\Sigma})$	Current dominant components
QSR	$(\omega,\,\omega)$	$(\omega,\,\omega)$	$(\omega,\,\omega)$	$(1,\,1)$	$(\omega^2,\,\omega^2)$	$(\omega^2,\,\omega^2)$	$\Re(\boldsymbol{j}_{\Lambda},\boldsymbol{j}_{H},\boldsymbol{j}_{\Sigma},\boldsymbol{m}_{\Lambda})$ $\Im(\boldsymbol{j}_{\Lambda},\boldsymbol{j}_{H},\boldsymbol{j}_{\Sigma},\boldsymbol{m}_{\Lambda})$
non-SED ECR	$(\omega^{3/2},\,\omega)$	$(\omega^2,\,\omega)$	$(\omega^2,\,\omega)$	$(\omega^2,\,\omega)$	$(\omega^2,\,\omega^{5/2})$	$(\omega^2,\,\omega^{5/2})$	$\Re(\boldsymbol{j}_{\Lambda},\boldsymbol{m}_{\Lambda},\boldsymbol{m}_{H},\boldsymbol{m}_{\Sigma})$ $\Im(\boldsymbol{j}_{\Lambda},\boldsymbol{j}_{H},\boldsymbol{j}_{\Sigma},\boldsymbol{m}_{\Lambda})$
SED ECR	$(\omega,\,\omega)$	$(\omega,\,\omega)$	$(\omega^2,\,\omega)$	$(\omega^2,\,\omega^2)$	$(\omega^2,\,\omega^2)$	$(\omega^2,\,\omega^2)$	$\Re(\boldsymbol{j}_{\Lambda},\boldsymbol{j}_{H},\boldsymbol{m}_{\Lambda},\boldsymbol{m}_{H},\boldsymbol{m}_{\Sigma})$ $\Im(\boldsymbol{j}_{\Lambda},\boldsymbol{j}_{H},\boldsymbol{j}_{\Sigma},\boldsymbol{m}_{\Lambda},\boldsymbol{m}_{H},\boldsymbol{m}_{\Sigma})$
(c) Electric interior near field							
Regime	$\boldsymbol{E}(\Re\boldsymbol{j}_{\Lambda})$ $\boldsymbol{E}(\Im\boldsymbol{j}_{\Lambda})$	$\boldsymbol{E}(\Re\boldsymbol{j}_{H})$ $\boldsymbol{E}(\Im\boldsymbol{j}_{H})$	$\boldsymbol{E}(\Re\boldsymbol{j}_{\Sigma})$ $\boldsymbol{E}(\Im\boldsymbol{j}_{\Sigma})$	$\boldsymbol{E}(\Re\boldsymbol{m}_{\Lambda})$ $\boldsymbol{E}(\Im\boldsymbol{m}_{\Lambda})$	$\boldsymbol{E}(\Re\boldsymbol{m}_{H})$ $\boldsymbol{E}(\Im\boldsymbol{m}_{H})$	$\boldsymbol{E}(\Re\boldsymbol{m}_{\Sigma})$ $\boldsymbol{E}(\Im\boldsymbol{m}_{\Sigma})$	Current dominant components
QSR	$(\omega^4,\,\omega^2)$ $(\omega^2,\,\omega^4)$	$(\omega^4,\,\omega^2)$ $(\omega^2,\,\omega^4)$	$(1,\,1)$ $(1,\,1)$	$(1,\,\omega^2)$ $(\omega^2,\,1)$	$(\omega^2,\,\omega^4)$ $(\omega^4,\,\omega^2)$	$(\omega^2,\,\omega^4)$ $(\omega^4,\,\omega^2)$	$\Re(\boldsymbol{j}_{\Sigma},\boldsymbol{m}_{\Lambda})$ $\Im(\boldsymbol{j}_{\Sigma},\boldsymbol{m}_{\Lambda})$
non-SED ECR	$(\omega^{7/2},\,\omega^{5/2})$ $(\omega^2,\,\omega^3)$	$(\omega^4,\,\omega^3)$ $(\omega^2,\,\omega^3)$	$(\omega^2,\,\omega^3)$ $(\omega^2,\,\omega)$	$(\omega^2,\,\omega^3)$ $(\omega^2,\,\omega)$	$(\omega^2,\,\omega^3)$ $(\omega^{7/2},\,\omega^{5/2})$	$(\omega^2,\,\omega^3)$ $(\omega^{7/2},\,\omega^{5/2})$	$\Im(\boldsymbol{j}_{\Sigma},\boldsymbol{m}_{\Lambda})$
SED ECR	$(\omega^2,\,\omega^2)$ $(\omega^2,\,\omega^2)$	$(\omega^2,\,\omega^2)$ $(\omega^2,\,\omega^2)$	$(\omega^3,\,\omega^3)$ $(\omega^2,\,\omega^2)$	$(\omega^2,\,\omega^2)$ $(\omega^2,\,\omega^2)$	$(\omega^2,\,\omega^2)$ $(\omega^2,\,\omega^2)$	$(\omega^2,\,\omega^2)$ $(\omega^2,\,\omega^2)$	$\Re(\boldsymbol{j}_{\Lambda},\boldsymbol{j}_{H},\boldsymbol{m}_{\Lambda},\boldsymbol{m}_{H},\boldsymbol{m}_{\Sigma})$ $\Im(\boldsymbol{j}_{\Lambda},\boldsymbol{j}_{H},\boldsymbol{j}_{\Sigma},\boldsymbol{m}_{\Lambda},\boldsymbol{m}_{H},\boldsymbol{m}_{\Sigma})$
(d) Magnetic interior near field							
Regime	$\boldsymbol{H}(\Re\boldsymbol{j}_{\Lambda})$ $\boldsymbol{H}(\Im\boldsymbol{j}_{\Lambda})$	$\boldsymbol{H}(\Re\boldsymbol{j}_{H})$ $\boldsymbol{H}(\Im\boldsymbol{j}_{H})$	$\boldsymbol{H}(\Re\boldsymbol{j}_{\Sigma})$ $\boldsymbol{H}(\Im\boldsymbol{j}_{\Sigma})$	$\boldsymbol{H}(\Re\boldsymbol{m}_{\Lambda})$ $\boldsymbol{H}(\Im\boldsymbol{m}_{\Lambda})$	$\boldsymbol{H}(\Re\boldsymbol{m}_{H})$ $\boldsymbol{H}(\Im\boldsymbol{m}_{H})$	$\boldsymbol{H}(\Re\boldsymbol{m}_{\Sigma})$ $\boldsymbol{H}(\Im\boldsymbol{m}_{\Sigma})$	Current dominant components
QSR	$(\omega,\,\omega^3)$ $(\omega^3,\,\omega)$	$(\omega,\,\omega^3)$ $(\omega^3,\,\omega)$	$(\omega,\,\omega^3)$ $(\omega^3,\,\omega)$	$(\omega,\,\omega)$ $(\omega,\,\omega)$	$(\omega^3,\,\omega^3)$ $(\omega^3,\,\omega^3)$	$(\omega^3,\,\omega)$ $(\omega,\,\omega^3)$	$\Re(\boldsymbol{j}_{\Lambda},\boldsymbol{j}_{H},\boldsymbol{j}_{\Sigma},\boldsymbol{m}_{\Lambda},\boldsymbol{m}_{\Sigma})$ $\Im(\boldsymbol{j}_{\Lambda},\boldsymbol{j}_{H},\boldsymbol{j}_{\Sigma},\boldsymbol{m}_{\Lambda},\boldsymbol{m}_{\Sigma})$
non-SED ECR	$(\omega^{3/2},\,\omega^{5/2})$ $(\omega^2,\,\omega)$	$(\omega^2,\,\omega^3)$ $(\omega^2,\,\omega)$	$(\omega^2,\,\omega^3)$ $(\omega^2,\,\omega)$	$(\omega^2,\,\omega^3)$ $(\omega^2,\,\omega)$	$(\omega^2,\,\omega^3)$ $(\omega^{7/2},\,\omega^{5/2})$	$(\omega^2,\,\omega)$ $(\omega^{3/2},\,\omega^{5/2})$	$\Re(\boldsymbol{m}_{\Sigma})$ $\Im(\boldsymbol{j}_{\Lambda},\boldsymbol{j}_{H},\boldsymbol{j}_{\Sigma},\boldsymbol{m}_{\Lambda})$
SED ECR	$(\omega,\,\omega)$ $(\omega,\,\omega)$	$(\omega,\,\omega)$ $(\omega,\,\omega)$	$(\omega^2,\,\omega^2)$ $(\omega,\,\omega)$	$(\omega,\,\omega)$ $(\omega,\,\omega)$	$(\omega,\,\omega)$ $(\omega,\,\omega)$	$(\omega,\,\omega)$ $(\omega,\,\omega)$	$\Re(\boldsymbol{j}_{\Lambda},\boldsymbol{j}_{H},\boldsymbol{m}_{\Lambda},\boldsymbol{m}_{H},\boldsymbol{m}_{\Sigma})$ $\Im(\boldsymbol{j}_{\Lambda},\boldsymbol{j}_{H},\boldsymbol{j}_{\Sigma},\boldsymbol{m}_{\Lambda},\boldsymbol{m}_{H},\boldsymbol{m}_{\Sigma})$
(e) Electric exterior near field							
Regime	$\boldsymbol{E}(\Re\boldsymbol{j}_{\Lambda})$ $\boldsymbol{E}(\Im\boldsymbol{j}_{\Lambda})$	$\boldsymbol{E}(\Re\boldsymbol{j}_{H})$ $\boldsymbol{E}(\Im\boldsymbol{j}_{H})$	$\boldsymbol{E}(\Re\boldsymbol{j}_{\Sigma})$ $\boldsymbol{E}(\Im\boldsymbol{j}_{\Sigma})$	$\boldsymbol{E}(\Re\boldsymbol{m}_{\Lambda})$ $\boldsymbol{E}(\Im\boldsymbol{m}_{\Lambda})$	$\boldsymbol{E}(\Re\boldsymbol{m}_{H})$ $\boldsymbol{E}(\Im\boldsymbol{m}_{H})$	$\boldsymbol{E}(\Re\boldsymbol{m}_{\Sigma})$ $\boldsymbol{E}(\Im\boldsymbol{m}_{\Sigma})$	Current dominant components
QSR	$(\omega^5,\,\omega^2)$ $(\omega^2,\,\omega^5)$	$(\omega^5,\,\omega^2)$ $(\omega^2,\,\omega^5)$	$(\omega^3,\,1)$ $(1,\,\omega^3)$	$(1,\,\omega^3)$ $(\omega^3,\,1)$	$(\omega^2,\,\omega^5)$ $(\omega^5,\,\omega^2)$	$(\omega^2,\,\omega^5)$ $(\omega^5,\,\omega^2)$	$\Re(\boldsymbol{j}_{\Sigma},\boldsymbol{m}_{\Lambda})$ $\Im(\boldsymbol{j}_{\Sigma},\boldsymbol{m}_{\Lambda})$
non-SED ECR	$(\omega^{11/2},\,\omega^{5/2})$ $(\omega^2,\,\omega^5)$	$(\omega^6,\,\omega^3)$ $(\omega^2,\,\omega^5)$	$(\omega^4,\,\omega)$ $(1,\,\omega^3)$	$(\omega^2,\,\omega^5)$ $(\omega^4,\,\omega)$	$(\omega^2,\,\omega^5)$ $(\omega^{11/2},\,\omega^{5/2})$	$(\omega^2,\,\omega^5)$ $(\omega^{11/2},\,\omega^{5/2})$	$\Im(\boldsymbol{j}_{\Sigma})$
SED ECR	$(\omega^5,\,\omega^2)$ $(\omega^2,\,\omega^5)$	$(\omega^5,\,\omega^2)$ $(\omega^2,\,\omega^5)$	$(\omega^4,\,\omega)$ $(1,\,\omega^3)$	$(\omega^2,\,\omega^5)$ $(\omega^5,\,\omega^2)$	$(\omega^2,\,\omega^5)$ $(\omega^5,\,\omega^2)$	$(\omega^2,\,\omega^5)$ $(\omega^5,\,\omega^2)$	$\Im(\boldsymbol{j}_{\Sigma})$
(f) Magnetic exterior near field							
Regime	$\boldsymbol{H}(\Re\boldsymbol{j}_{\Lambda})$ $\boldsymbol{H}(\Im\boldsymbol{j}_{\Lambda})$	$\boldsymbol{H}(\Re\boldsymbol{j}_{H})$ $\boldsymbol{H}(\Im\boldsymbol{j}_{H})$	$\boldsymbol{H}(\Re\boldsymbol{j}_{\Sigma})$ $\boldsymbol{H}(\Im\boldsymbol{j}_{\Sigma})$	$\boldsymbol{H}(\Re\boldsymbol{m}_{\Lambda})$ $\boldsymbol{H}(\Im\boldsymbol{m}_{\Lambda})$	$\boldsymbol{H}(\Re\boldsymbol{m}_{H})$ $\boldsymbol{H}(\Im\boldsymbol{m}_{H})$	$\boldsymbol{H}(\Re\boldsymbol{m}_{\Sigma})$ $\boldsymbol{H}(\Im\boldsymbol{m}_{\Sigma})$	Current dominant components
QSR	$(\omega,\,\omega^4)$ $(\omega^4,\,\omega)$	$(\omega,\,\omega^4)$ $(\omega^4,\,\omega)$	$(\omega,\,\omega^4)$ $(\omega^4,\,\omega)$	$(\omega^4,\,\omega)$ $(\omega,\,\omega^4)$	$(\omega^6,\,\omega^3)$ $(\omega^3,\,\omega^6)$	$(\omega^4,\,\omega)$ $(\omega,\,\omega^4)$	$\Re(\boldsymbol{j}_{\Lambda},\boldsymbol{j}_{H},\boldsymbol{j}_{\Sigma},\boldsymbol{m}_{\Lambda},\boldsymbol{m}_{\Sigma})$ $\Im(\boldsymbol{j}_{\Lambda},\boldsymbol{j}_{H},\boldsymbol{j}_{\Sigma},\boldsymbol{m}_{\Lambda},\boldsymbol{m}_{\Sigma})$
non-SED ECR	$(\omega^{3/2},\,\omega^{9/2})$ $(\omega^4,\,\omega)$	$(\omega^2,\,\omega^5)$ $(\omega^4,\,\omega)$	$(\omega^2,\,\omega^5)$ $(\omega^4,\,\omega)$	$(\omega^6,\,\omega^3)$ $(\omega^2,\,\omega^5)$	$(\omega^6,\,\omega^3)$ $(\omega^{7/2},\,\omega^{13/2})$	$(\omega^4,\,\omega)$ $(\omega^{3/2},\,\omega^{9/2})$	$\Re(\boldsymbol{m}_{\Sigma})$ $\Im(\boldsymbol{j}_{\Lambda},\boldsymbol{j}_{H},\boldsymbol{j}_{\Sigma})$
SED ECR	$(\omega,\,\omega^4)$ $(\omega^4,\,\omega)$	$(\omega,\,\omega^4)$ $(\omega^4,\,\omega)$	$(\omega^2,\,\omega^5)$ $(\omega^4,\,\omega)$	$(\omega^6,\,\omega^3)$ $(\omega^3,\,\omega^6)$	$(\omega^6,\,\omega^3)$ $(\omega^3,\,\omega^6)$	$(\omega^4,\,\omega)$ $(\omega,\,\omega^4)$	$\Re(\boldsymbol{j}_{\Lambda},\boldsymbol{j}_{H},\boldsymbol{m}_{\Sigma})$ $\Im(\boldsymbol{j}_{\Lambda},\boldsymbol{j}_{H},\boldsymbol{j}_{\Sigma},\boldsymbol{m}_{\Sigma})$
(g) Rescaled current density							
Regime	$b_R^{-1}\boldsymbol{j}_{\Lambda}$	$a_R^{-1}\boldsymbol{j}_{H}$	$a_R^{-1}\boldsymbol{j}_{\Sigma}$	$d_R^{-1}\boldsymbol{m}_{\Lambda}$	$c_R^{-1}\boldsymbol{m}_{H}$	$c_R^{-1}\boldsymbol{m}_{\Sigma}$	Recovered components
QSR	$(1,1)$	$(1,1)$	$(1,1)$	$(1,1)$	$(1,1)$	$(1,1)$	$\Re(\boldsymbol{j}_{\Lambda},\boldsymbol{j}_{H},\boldsymbol{j}_{\Sigma},\boldsymbol{m}_{\Lambda},\boldsymbol{m}_{H},\boldsymbol{m}_{\Sigma})$ $\Im(\boldsymbol{j}_{\Lambda},\boldsymbol{j}_{H},\boldsymbol{j}_{\Sigma},\boldsymbol{m}_{\Lambda},\boldsymbol{m}_{H},\boldsymbol{m}_{\Sigma})$
non-SED ECR	$(\omega^2,\omega^{3/2})$	$(\omega^{5/2},\omega^{3/2})$	$(\omega^{5/2},\omega^{3/2})$	$(\omega^{5/2},\omega^{3/2})$	$(\omega^{3/2},\omega^2)$	$(\omega^{3/2},\omega^2)$	$\Re(\boldsymbol{j}_{\Lambda},\boldsymbol{m}_{H},\boldsymbol{m}_{\Sigma})$ $\Im(\boldsymbol{j}_{\Lambda},\boldsymbol{j}_{H},\boldsymbol{j}_{\Sigma},\boldsymbol{m}_{\Lambda})$
SED ECR	$(\omega^{3/2},\omega^{3/2})$	$(\omega^{3/2},\omega^{3/2})$	$(\omega^{5/2},\omega^{3/2})$	$(\omega^{3/2},\omega^{3/2})$	$(\omega^{3/2},\omega^{3/2})$	$(\omega^{3/2},\omega^{3/2})$	$\Re(\boldsymbol{j}_{\Lambda},\boldsymbol{j}_{H},\boldsymbol{m}_{\Lambda},\boldsymbol{m}_{H},\boldsymbol{m}_{\Sigma})$ $\Im(\boldsymbol{j}_{\Lambda},\boldsymbol{j}_{H},\boldsymbol{j}_{\Sigma},\boldsymbol{m}_{\Lambda},\boldsymbol{m}_{H},\boldsymbol{m}_{\Sigma})$

V. PRECONDITIONING OF THE PMCHWT IN SEVERAL LOW-FREQUENCY REGIMES

This section aims at defining a preconditioned formulation of the PMCHWT equation with the following objectives: 1) stabilizing the condition number with respect to both the electrical length and the conductivity of the scatterer in the regimes analyzed above and 2) preventing the loss of dominant components of the current in the low-frequency limit, in order to guarantee the accuracy of the solution and fields. This can be obtained by properly rescaling the quasi-Helmholtz decomposed components of the system, by means of primal and dual quasi-Helmholtz projectors. We propose here a quasi-Helmholtz projectors based preconditioning strategy tailored to

TABLE III
SCALAR MULTIPLICATIVE COEFFICIENTS DEFINING THE PROPOSED PRECONDITIONING STRATEGY

	QSR-ind	QSR-cap	non-SED ECR-ind	non-SED ECR-cap	SED ECR-ind	SED ECR-cap
a_L	1	χ^{-2}	$\chi^{1/2}\gamma^{-1}$	$\chi^{-1/2}$	$\chi^{-1/2}$	$\chi^{-1/2}$
b_L	χ^{-2}	1	$\chi^{-1/2}$	$\chi^{3/2}$	$\chi^{-1/2}$	$\chi^{3/2}$
c_L	χ^{-1}	χ^{-1}	$\chi^{1/2}$	$\chi^{1/2}$	$\gamma^{1/2}$	$\gamma^{1/2}$
d_L	χ^{-1}	χ^{-1}	$\chi^{-1/2}\gamma$	$\chi^{1/2}$	$\gamma^{1/2}$	$\gamma^{1/2}$
a_R	χ	χ	$\chi^{-1/2}$	$\chi^{-1/2}$	$\chi^{-1/2}$	$\chi^{-1/2}$
b_R	χ	χ	$\chi^{1/2}\gamma$	$\chi^{-1/2}$	$\chi^{3/2}$	$\chi^{-1/2}$
c_R	1	χ^2	$\chi^{-1/2}\gamma$	$\chi^{1/2}$	$\gamma^{1/2}$	$\gamma^{1/2}$
d_R	χ^2	1	$\chi^{1/2}$	$\chi^{-3/2}\gamma^2$	$\gamma^{1/2}$	$\gamma^{1/2}$

the magnetic frill (or loop) excitations analyzed in Tables I and II, referred to as excitations of inductive (ind.) or capacitive (cap.) types. The proposed formulation follows from a left-right preconditioning of the original one, i.e.,

$$\boldsymbol{LZRy} = \boldsymbol{L}\begin{pmatrix}\boldsymbol{e}\\ \boldsymbol{h}\end{pmatrix} \tag{64}$$

where the left and right preconditioning matrices take the form

$$\boldsymbol{L} = \begin{cases}\begin{pmatrix}\frac{1}{\sqrt{\eta_0}}\boldsymbol{G}^{-\mathrm{T}}\mathbb{M}_{\mathrm{up}}\boldsymbol{G}^{-1} & \boldsymbol{0}\\ \boldsymbol{0} & \sqrt{\eta_0}\boldsymbol{G}^{-\mathrm{T}}\mathbb{M}_{\mathrm{low}}\boldsymbol{G}^{-1}.\end{pmatrix} & \text{ind. type}\\ \begin{pmatrix}\frac{1}{\sqrt{\eta_0}}\boldsymbol{M}_{\mathrm{up}} & \boldsymbol{0}\\ \boldsymbol{0} & \sqrt{\eta_0}\boldsymbol{M}_{\mathrm{low}}.\end{pmatrix} & \text{cap. type}\end{cases} \tag{65}$$

$$\boldsymbol{R} = \begin{cases}\begin{pmatrix}\frac{1}{\sqrt{\eta_0}}\boldsymbol{M}_{\mathrm{left}} & \boldsymbol{0}\\ \boldsymbol{0} & \sqrt{\eta_0}\boldsymbol{M}_{\mathrm{right}}.\end{pmatrix} & \text{ind. type}\\ \begin{pmatrix}\frac{1}{\sqrt{\eta_0}}\mathbb{G}^{-1}\mathbb{M}_{\mathrm{left}}\mathbb{G}^{-\mathrm{T}} & \boldsymbol{0}\\ \boldsymbol{0} & \sqrt{\eta_0}\mathbb{G}^{-1}\mathbb{M}_{\mathrm{right}}\mathbb{G}^{-\mathrm{T}}.\end{pmatrix} & \text{cap. type.}\end{cases} \tag{66}$$

As already noticed in Section IV-D, the frequency behavior of the harmonic component of the electric field produced by a magnetic frill is different in case the excitation is of inductive or capacitive type. To correctly enforce the required cancellations, we employ two different and symmetric, preconditioning strategies for the inductive and capacitive cases [(65) and (66)]. Indeed, the use of dual projectors in the left preconditioning matrix and primal projectors in the right preconditioning matrix for inductive excitations, and vice versa for capacitive excitations, allows to correctly enforce the cancellation of the static part of the electric component of the RHS projected on the rotated nonsolenoidal subspace, nonincluding the quasi-harmonic subspace, if the excitation is of inductive type, and the cancellation of the static part of the electric component of the RHS projected on the solenoidal subspace, including the quasi-harmonic subspace, if the excitation is capacitive.

The preconditioning blocks used for inductive type excitations are

$$\mathbb{M}_{\mathrm{up}} = a_L\,\mathbb{P}^{\Sigma\boldsymbol{H}} + b_L\,\mathbb{P}^{\Lambda} \tag{67}$$

$$\mathbb{M}_{\mathrm{low}} = c_L\,\mathbb{P}^{\Sigma\boldsymbol{H}} + d_L\,\mathbb{P}^{\Lambda} \tag{68}$$

$$\boldsymbol{M}_{\mathrm{left}} = a_R\,\boldsymbol{P}^{\Lambda\boldsymbol{H}} + b_R\,\boldsymbol{P}^{\Sigma} \tag{69}$$

$$\boldsymbol{M}_{\mathrm{right}} = c_R\,\boldsymbol{P}^{\Lambda\boldsymbol{H}} + d_R\,\boldsymbol{P}^{\Sigma}. \tag{70}$$

Symmetrically, the ones used in case of capacitive type excitations are

$$\boldsymbol{M}_{\mathrm{up}} = a_L\,\boldsymbol{P}^{\Lambda\boldsymbol{H}} + b_L\,\boldsymbol{P}^{\Sigma} \tag{71}$$

$$\boldsymbol{M}_{\mathrm{low}} = c_L\,\boldsymbol{P}^{\Lambda\boldsymbol{H}} + d_L\,\boldsymbol{P}^{\Sigma} \tag{72}$$

$$\mathbb{M}_{\mathrm{left}} = a_R\,\mathbb{P}^{\Sigma\boldsymbol{H}} + b_R\,\mathbb{P}^{\Lambda} \tag{73}$$

$$\mathbb{M}_{\mathrm{right}} = c_R\,\mathbb{P}^{\Sigma\boldsymbol{H}} + d_R\,\mathbb{P}^{\Lambda}. \tag{74}$$

The scalar coefficients $\{a_L - \mathrm{d_R}\}$ should be set as a function of the frequency-conductivity regime considered, in order to stabilize the formulation with respect to the frequency and the conductivity independently.

The coefficients to be used in case of inductive and capacitive excitations are reported in Table III. In addition, arguments justifying these choices are delineated in the following.

The conditioning analysis of the preconditioned formulation will be based on the asymptotic scalings of the loop-star decomposition of the preconditioned matrix, defined as

$$\boldsymbol{Z}_{P,\Lambda\boldsymbol{H}\Sigma} \coloneqq \begin{pmatrix}\boldsymbol{A}^{\mathrm{T}} & \boldsymbol{0}\\ \boldsymbol{0} & \boldsymbol{A}^{\mathrm{T}}\end{pmatrix}\boldsymbol{LZR}\begin{pmatrix}\boldsymbol{A} & \boldsymbol{0}\\ \boldsymbol{0} & \boldsymbol{A}\end{pmatrix}. \tag{75}$$

A. Quasi-Static Regime

In the QSR, the contribution of losses inside the material does not influence the overall scalings of the quasi-Helmholtz decomposed formulation. Indeed, the loop-star decomposition identified in (38) corresponds to the one of the PMCHWT equation applied to lossless dielectric media, already identified in [12].

1) Inductive Type Excitation: Different sets of coefficients allow for frequency and conductivity preconditioning of the formulation. One classical choice [12] is for example

$$a_L = c_L = b_R = d_R = \chi^{1/2} \text{ and } b_L = d_L = a_R = c_R = \chi^{-1/2}$$

leading to the loop-star decomposition

$$\boldsymbol{Z}_{P,\Lambda\boldsymbol{H}\Sigma} = \mathcal{O}\begin{pmatrix}1 & 1 & \chi & \chi & \chi & 1\\ \chi & \chi & \chi^2 & \chi^2 & 1 & \chi\\ \chi & \chi & 1 & 1 & 1 & \chi\\ \chi & \chi & 1 & 1 & 1 & \chi\\ \chi^2 & 1 & \chi & \chi & \chi & \chi^2\\ 1 & 1 & \chi & \chi & \chi & 1\end{pmatrix} \tag{76}$$

leading to a constant condition number behavior in the low-frequency limit [12].

However, for the kind of excitation considered here, this choice would not allow for the preservation of all the relevant current components. Indeed, the components $\boldsymbol{j}_\Lambda$, $\boldsymbol{j}_H$, and $\boldsymbol{m}_\Sigma$, both in their real and imaginary parts, which are useful to reconstruct the magnetic field inside and outside the scatterer, would be lost in numerical cancellation in the low-frequency limit.

To preserve the accuracy of all the required current components, we opt instead to the choice of coefficients reported in Table III, resulting in the loop-star decomposition

$$\boldsymbol{Z}_{P,\Lambda\boldsymbol{H}\Sigma} = \mathcal{O}\begin{pmatrix} 1 & 1 & 1 & 1 & 1 & 1 \\ \chi^2 & \chi^2 & \chi^2 & \chi^2 & 1 & \chi^2 \\ \chi^2 & \chi^2 & 1 & 1 & 1 & \chi^2 \\ \chi^2 & \chi^2 & 1 & 1 & 1 & \chi^2 \\ \chi^2 & 1 & 1 & 1 & 1 & \chi^2 \\ 1 & 1 & 1 & 1 & 1 & 1 \end{pmatrix} \tag{77}$$

indicating the favorable condition properties of the preconditioned matrix and that the matrix has a well-defined low-frequency limit converging to the static problem. The preserved current components correspond to the ones needed for the correct fields reconstruction, as shown in Table I.

2) Capacitive Type Excitation: Similarly as above, we determine from Table I the components to be preserved and design the multiplicative preconditioner accordingly. Our choice of coefficients, in Table III, results in

$$\boldsymbol{Z}_{P,\Lambda\boldsymbol{H}\Sigma} = \mathcal{O}\begin{pmatrix} 1 & 1 & 1 & 1 & \chi^2 & 1 \\ 1 & 1 & 1 & 1 & 1 & 1 \\ \chi^2 & \chi^2 & 1 & 1 & \chi^2 & \chi^2 \\ \chi^2 & \chi^2 & 1 & 1 & \chi^2 & \chi^2 \\ \chi^2 & 1 & 1 & 1 & \chi^2 & \chi^2 \\ 1 & 1 & 1 & 1 & \chi^2 & 1 \end{pmatrix} \tag{78}$$

which indicates that the resulting matrix has favorable conditioning properties, and allows to preserve the required current components (see Table II).

B. Nonskin-Effect-Dominated Eddy-Current Regime

1) Inductive-Type Excitation: One first intuitive choice for the scalar coefficients $\{a_L - \mathrm{d_R}\}$ is

$$a_L = c_L = b_R = d_R = \chi^{1/2}, \qquad b_L = a_R = \chi^{-1/2},$$
$$\text{and } d_L = c_R = \chi^{-1/2}\gamma.$$

This would allow to retrieve all the dominant current components. Moreover, this would result in the decomposition

$$\boldsymbol{Z}_{P,\Lambda\boldsymbol{H}\Sigma} = \mathcal{O}\begin{pmatrix} 1 & 1 & \chi & \xi & \xi & 1 \\ \chi & \chi & \chi^2 & \chi\xi & \gamma & \chi \\ \chi & \chi & 1 & \gamma & \gamma & \chi \\ \xi & \xi & \gamma & 1 & 1 & \xi \\ \xi^2 & 1 & \chi & \xi & \xi & \xi^2 \\ 1 & 1 & \chi & \xi & \xi & 1. \end{pmatrix}. \tag{79}$$

In the presence of multiply connected geometries with finite genus g instead, the preconditioned matrices exhibit a finite-dimensional nullspace in the static limit, of size $2g$. This can be seen for example by studying the loop-star decomposition for a genus-1 geometry and separating the toroidal from the poloidal global loop contributions (see [24] for further details on this technique), i.e., by replacing matrix $\boldsymbol{A}$ with $\boldsymbol{A}' := (\Lambda \quad \boldsymbol{H}^T \quad \boldsymbol{H}^P \quad \Sigma)$, where $\boldsymbol{H}^T$ and $\boldsymbol{H}^P$ are the transformation matrices from the toroidal and poloidal global loops to the RWG subspace. The decomposition of the preconditioned matrix reads

$$\begin{pmatrix} \boldsymbol{A}'^{\mathrm{T}} & \boldsymbol{0} \\ \boldsymbol{0} & \boldsymbol{A}'^{\mathrm{T}} \end{pmatrix} \boldsymbol{LZR} \begin{pmatrix} \boldsymbol{A}' & \boldsymbol{0} \\ \boldsymbol{0} & \boldsymbol{A}' \end{pmatrix}$$
$$= \mathcal{O}\begin{pmatrix} 1 & 1 & 1 & \chi & \xi & \xi & \xi & 1 \\ \chi & \chi & \chi & \chi^2 & \chi\xi & \boldsymbol{\xi^2\gamma} & \gamma & \chi \\ \chi & \chi & \chi & \chi^2 & \chi\xi & \boldsymbol{\xi^2\gamma} & \boldsymbol{\xi^2\gamma} & \chi \\ \chi & \chi & \chi & 1 & \gamma & \gamma & \gamma & \chi \\ \xi & \xi & \xi & \gamma & 1 & 1 & 1 & \xi \\ \xi^2 & \boldsymbol{\xi^2} & 1 & \chi & \xi & \xi & \xi & \xi^2 \\ \xi^2 & \boldsymbol{\xi^2} & \boldsymbol{\xi^2} & \chi & \xi & \xi & \xi & \xi^2 \\ 1 & 1 & 1 & \chi & \xi & \xi & \xi & 1 \end{pmatrix} \tag{80}$$

where the terms in bold take into account the fact that the static part of the MFIO matrix vanishes when the basis loop does not pass through the test loop [24]. The application of (80) to the V-dimensional (with V denoting the number of vertices of the mesh) space of magnetic currents composed of local RWG loops and the toroidal global loop, that is, the vector

$$\left(\boldsymbol{0}\ \boldsymbol{0}\ \boldsymbol{0}\ \boldsymbol{0}\ \boldsymbol{m}_\Lambda\ \boldsymbol{m}_{\boldsymbol{H}^T}\ \boldsymbol{0}\ \boldsymbol{0}\right)^{\mathrm{T}} \tag{81}$$

results in

$$\left(\mathcal{O}(\xi)\ \mathcal{O}(\chi\xi)\ \mathcal{O}(\chi\xi)\ \mathcal{O}(\gamma)\ \boldsymbol{v}\ \mathcal{O}(\xi)\ \mathcal{O}(\xi)\ \mathcal{O}(\xi)\right)^{\mathrm{T}} \tag{82}$$

where $\boldsymbol{v}$ is given by the product between a rank-deficient $(V-1)\times V$ block and the V-dimensional current. As $\chi \ll 1$, $\gamma \ll 1$, and $\xi \ll 1$ in the non-SED ECR, the nullspace of such rank-deficient block corresponds to the nullspace of the entire matrix in the low-frequency limit. Similar results hold for the $V-$dimensional magnetic current space composed of local RWG loops and the poloidal global loop, resulting, overall, in a 2-D nullspace of the preconditioned formulation, which, numerically, takes the form of two isolated singular values decaying toward lower frequencies. Note that a similar analysis applied to the preconditioned formulation in the QSR confirms the absence of a nullspace related to the global loops of the geometry.

To remove the artificial nullspace introduced by this suboptimal preconditioning, we further manipulate the set of coefficients $\{a_L - \mathrm{d_R}\}$. The choice reported in Table III on the one hand allows the retrieval of all the useful current components—as shown in Table I—and on the other hand results in the behavior

$$\boldsymbol{Z}_{P,\Lambda\boldsymbol{H}\Sigma} = \mathcal{O}\begin{pmatrix} 1 & 1 & \chi\gamma & \xi & \xi & 1 \\ \xi & \xi & \chi^2 & \xi^2 & 1 & \xi \\ \xi & \xi & 1 & 1 & 1 & \xi \\ \xi & \xi & \gamma^2 & 1 & 1 & \xi \\ \xi^2 & 1 & \chi\gamma & \xi & \xi & \xi^2 \\ 1 & 1 & \chi\gamma & \xi & \xi & 1 \end{pmatrix} \tag{83}$$

indicating favorable conditioning properties. Moreover, by applying an analysis similar to the one above, the absence of

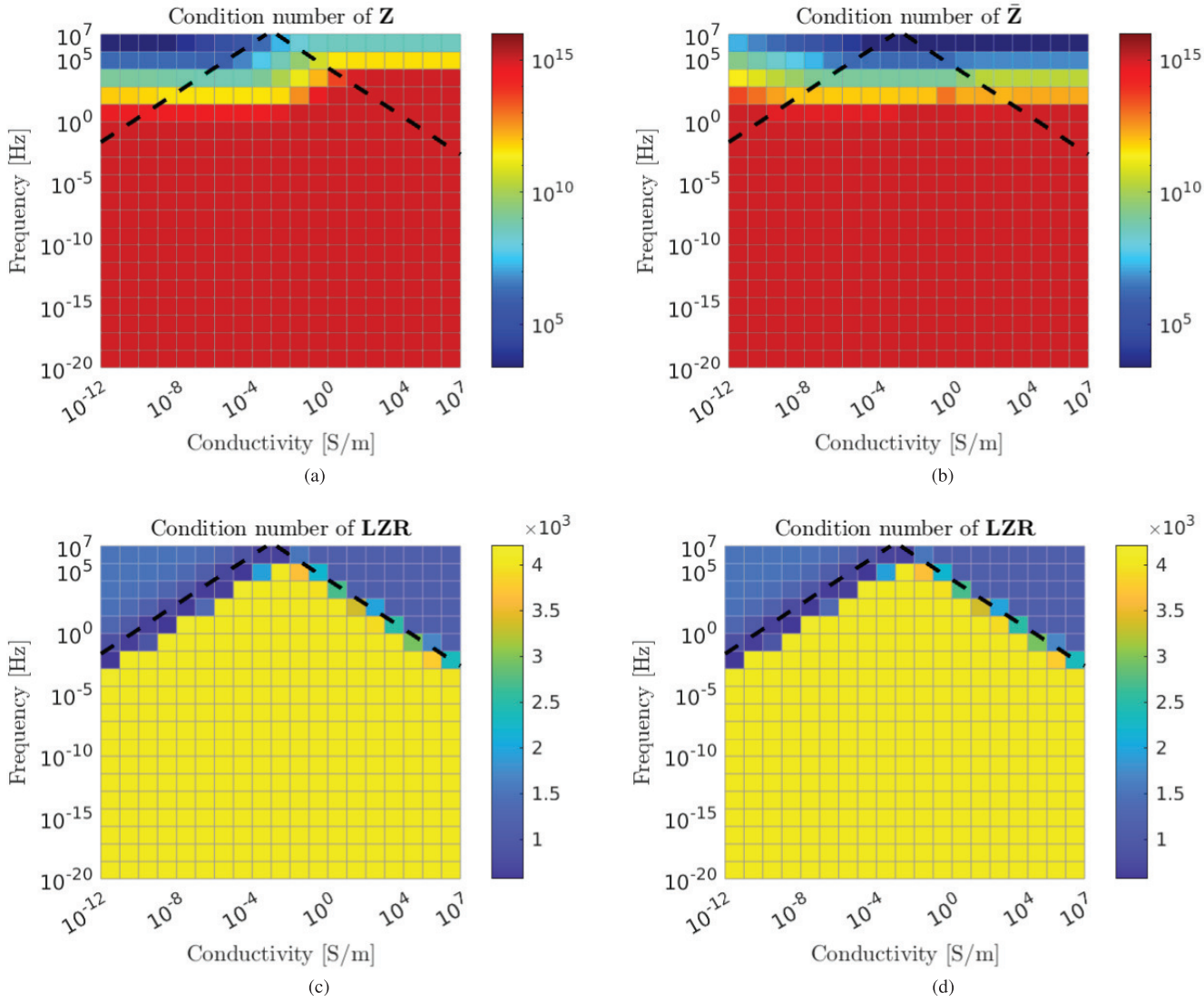

Fig. 3. Condition number of $\boldsymbol{Z}$ (a), $\bar{Z}$ (b) and $\boldsymbol{LZR}$ (c, d) evaluated over a torus with major and minor radii of 1 m and 0.3 m discretized at $h \simeq 0.44$ m. The preconditioning applied is tailored to inductive (c) and capacitive (d) excitations.

a nullspace in the low-frequency limit related to the non-zero genus of the geometry can be verified.

2) Capacitive-Type Excitation: An effective choice of coefficients to retrieve all the useful current components is the one reported in Table III, resulting in the loop-star decomposition

$$\boldsymbol{Z}_{P,\Lambda\boldsymbol{H}\Sigma} = \mathcal{O} \begin{pmatrix} 1 & 1 & 1 & 1 & \xi^2 & 1 \\ 1 & 1 & 1 & 1 & 1 & 1 \\ \chi^2 & \chi^2 & 1 & \gamma^2 & \chi^2 & \chi^2 \\ \xi^2 & \xi^2 & 1 & 1 & \xi^2 & \xi^2 \\ \xi^2 & 1 & 1 & 1 & \xi^2 & \xi^2 \\ 1 & 1 & 1 & 1 & \xi^2 & 1 \end{pmatrix} \tag{84}$$

indicating that the formulation has a well-defined low-frequency limit and favorable conditioning properties.

C. Skin-Effect-Dominated Eddy-Current Regime

1) Inductive-Type Excitation: As indicated in Table I, all the current components, in real and imaginary parts, are required to correctly retrieve the fields in the low-frequency limit. This requirement is satisfied by the choice of coefficients in Table III, resulting in the following behavior of the loop-star decomposed system:

$$\boldsymbol{Z}_{P,\Lambda\boldsymbol{H}\Sigma} = \mathcal{O} \begin{pmatrix} 1 & 1 & \chi^2 & \xi^{-1/2} & \xi^{-1/2} & \xi^{-1/2} \\ 1 & 1 & \chi^2 & \xi^{-1/2} & \xi^{-1/2} & \xi^{-1/2} \\ 1 & 1 & 1 & \xi^{-1/2} & \xi^{-1/2} & \xi^{-1/2} \\ \xi^{-1/2} & \xi^{-1/2} & \chi^{3/2}\gamma^{1/2} & 1 & 1 & 1 \\ \xi^{-1/2} & \xi^{-1/2} & \chi^{3/2}\gamma^{1/2} & 1 & 1 & 1 \\ \xi^{-1/2} & \xi^{-1/2} & \chi^{3/2}\gamma^{1/2} & 1 & 1 & 1 \end{pmatrix} \tag{85}$$

attesting to the favorable conditioning properties of the formulation.

2) Capacitive-Type Excitation: In this case, the preconditioning strategy implemented for the inductive-type excitation can be symmetrized, by exchanging the role of left and right coefficients (see Table III), resulting in the same preconditioned formulation as in (85), which also allows for the retrieval of the required current components.

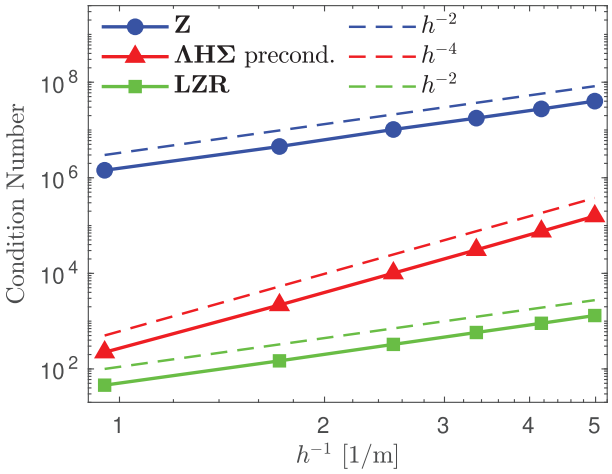

Fig. 4. Condition number of the formulations applied to a sphere of radius 1 m of conductivity 10 S/m excited at 1×10^5 Hz at different mesh refinements: comparison between the original PMCHWT formulation ($\boldsymbol{Z}$), the loop-star preconditioned formulation ($\Lambda\boldsymbol{H}\Sigma$ precond.), and this work ($\boldsymbol{LZR}$).

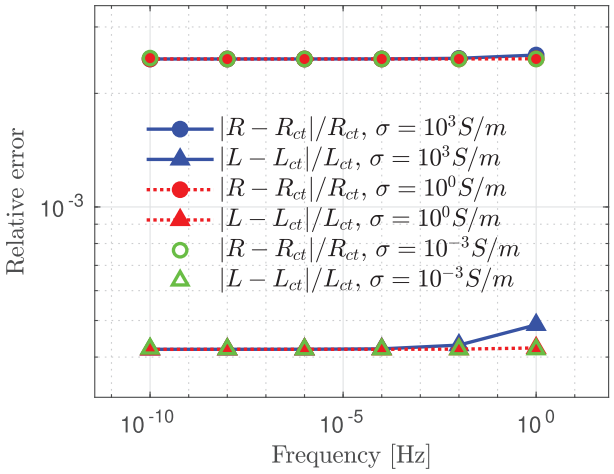

Fig. 5. Full-wave evaluation of the impedance of a toroidal structure with major and minor radii of 1 and 0.2 m of different conductivities: relative difference with respect to circuit theory expectations R_{ct} and L_{ct}.

Note that the asymptotic analyses of the loop-star decomposed preconditioned systems shown above in (77), (78), (83), (84), and (85) provide an indication of the favorable conditioning properties of the preconditioned system, but cannot provide a formal answer to the question of whether or not the low-frequency limit of the preconditioned matrices suffer from a finite dimensional nullspace. Nevertheless, numerical results presented in Section VI [see Fig. 3(c) and (d)] suggest the well-posedness and stability of the proposed formulations.

VI. Numerical Results

In this section, numerical results will illustrate the favorable spectral properties, the stability, and the accuracy of the proposed formulation. First, the proposed formulation is applied to a multiply connected toroidal structure and its condition number is compared to that of the PMCHWT equation (matrix $\boldsymbol{Z}$) and of its rescaled version (matrix $\bar{Z}$) in a wide range of conductivities and frequencies (always in the low-frequency regime), both for inductive and capacitive-type excitation versions (Fig. 3). On the one hand the low-frequency breakdown of the standard PMCHWT matrices $\boldsymbol{Z}$ or $\bar{Z}$ is clear (as well as other conductivity related instabilities mentioned above), on the other hand the stability of the proposed formulation, that exhibits a condition number that remains constant in frequency and conductivity in the three regimes considered. To produce these results, we applied the preconditioning strategies proposed for the QSR, non-SED ECR, and SED ECR in the corresponding frequency and conductivity regions, identified by (34), (39), and (44) by substituting the symbols $\gg$, $\ll$ with $>$, $<$. The demarcation between these regions has been marked with black dotted lines.

Next, we verify that the quasi-Helmholtz projectors based preconditioning does not degrade the spectral properties of the formulation with respect to mesh refinement by comparing the condition number of the standard PMCHWT matrix and of the proposed formulation with the one of a PMCHWT formulation preconditioned with a loop-star approach. The rescaling coefficients employed in the loop-star preconditioning are the same as the one used in our formulation, in Table III. The results, presented in Fig. 4, show that the condition number of matrix $\boldsymbol{Z}$ and the new formulation based on quasi-Helmholtz projector increase as h^{-2} with refinement, which confirms the fact that the use of quasi-Helmholtz preconditioning is not detrimental with respect to the PMCHWT dense discretization breakdown. The condition number of the loop-star preconditioned formulation, instead, grows as h^{-4}.

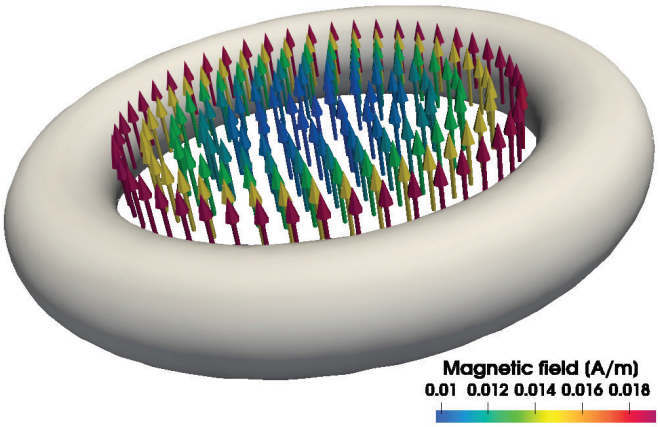

Fig. 6. Torus of major and minor radii of 1 and 0.2 m of conductivity 1 S/m excited by a magnetic frill imposing 1 V at 10 mHz: induced magnetic field.

Beyond the conditioning properties of the equations under study, we next need to assess their accuracy. We consider two canonical circuital structures and employ our full-wave solver to evaluate their impedance, of both inductive and capacitive type. These values, derived from the voltages and currents themselves computed from the simulated total fields, are then compared to the values predicted from circuit theory to verify the accuracy of the schemes. The following results were obtained with a direct solver.

The first structure considered is a torus with major and minor radii $R_M = 1$ m and $R_m = 0.2$ m excited by an inductive magnetic frill passing through the global toroidal loop of the

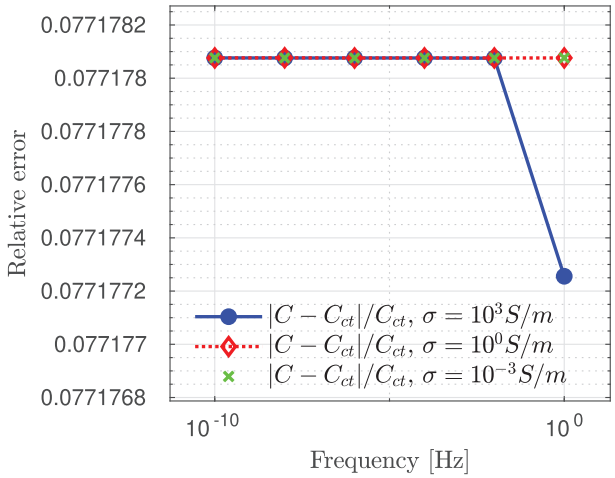

Fig. 7. Full-wave evaluation of the impedance of a capacitive structure with circular parallel plates of radius 4 m at distance 0.2 m of different conductivities: relative difference with respect to circuit theory expectation C_{ct}.

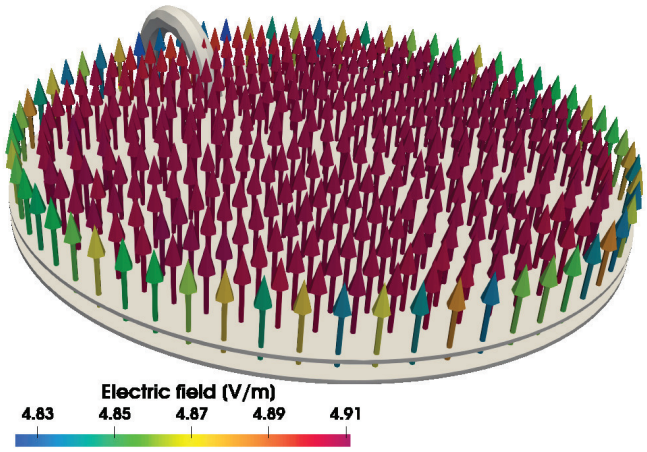

Fig. 8. Capacitive structure with circular parallel plates of radius 4 m at distance 0.2 m of conductivity 1×10^{-3} S/m excited by a magnetic frill imposing 1 V at 1 Hz: electric field between the plates.

geometry, which imposes a potential difference of 1 V.The conductivity of the toroidal body Ω varies from 1×10^{-3} S/m to 1×10^{3} S/m. We estimate the resistance and inductance of the circuit from the electromagnetic field scattered by the equivalent currents retrieved from the solution of our formulation and compare these values with the approximation valid in low frequency for conductors with uniform cross-section $R_{ct} := 2R_M/(R_m^2\sigma)$ [30], and $L_{ct} \simeq 1.807\ \mu$H [31, eq. 4.27]. The relative difference between the results obtained from our full-wave formulation and the ones known from circuit theory, R_{ct} and L_{ct}, is reported in Fig. 5 for a wide range of frequencies. In particular, the relative error of the resistance is approximately 2.5×10^{-3}, the one of the inductance 4.2×10^{-4}, both of them independently of frequency and conductivity of the line. Fig. 6 represents the magnetic field induced by the current circulating in the loop. This induced field is parallel to the torus axis and symmetric with respect to the center.

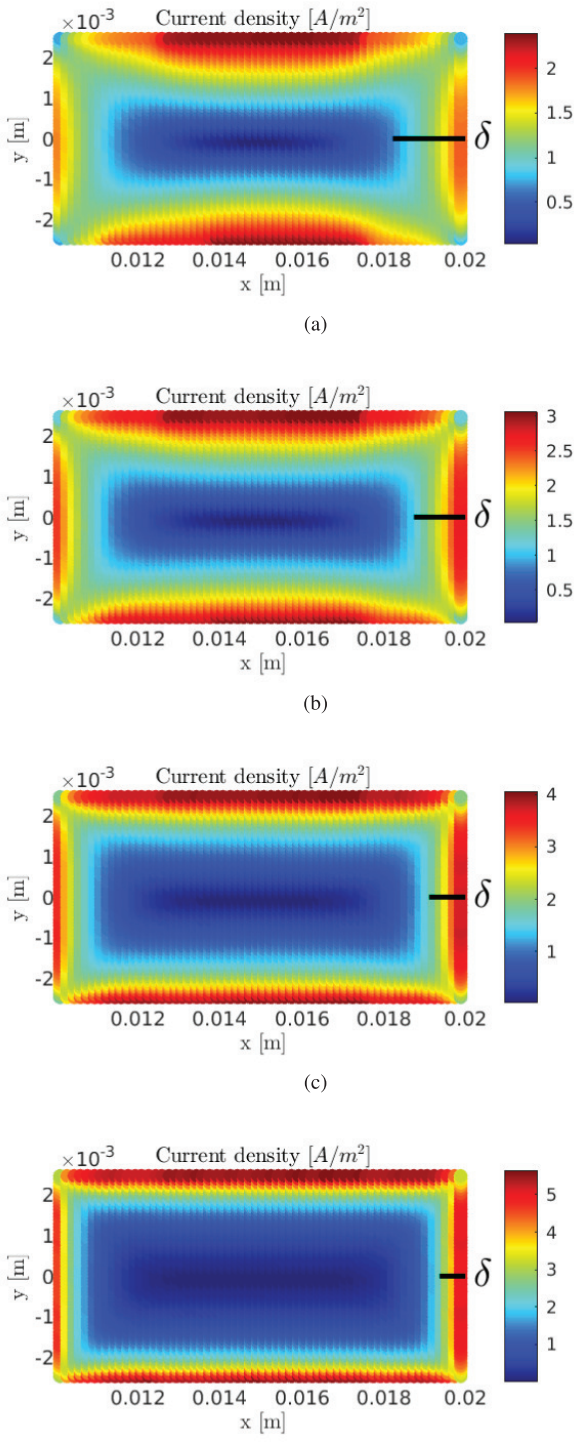

Fig. 9. Electric current density inside a rectangular cross section of sides 1 and 0.5 cm of conductivity 1×10^{7} S/m excited by an impinging plane wave traveling along $\hat{y}$ at frequencies. (a) 8 kHz. (b) 16 kHz. (c) 32 kHz. (d) 64 kHz.

The second structure instead is a parallel plates capacitor, made up of a couple of circular parallel plates of radius $R_p = 4$ m placed at distance $d = 0.2$ m. The plates are connected by a wire of circular cross section of radius 0.2 m. A potential difference of 1 V is imposed across the plates using

a capacitive magnetic frill around this wire. The capacitance of the structure is computed from the simulated fields, and compared to the value of capacitance expected from circuit theory $C_{ct} \coloneqq \epsilon_0 \pi R_p^2/d$ in a wide range of frequencies and conductivities of the circuit. The results are summarized in Fig. 7, showing a relative difference between the two values of capacitance of approximately 7.7×10^{-2}, irrespectively of frequency and conductivity. Fig. 8 shows a representation of the electric field generated between the plates. This electric field is normally directed and uniform at a value near to 5 V/m.

In the final numerical example, we demonstrate that our formulation can effectively track the field penetration depth variation inside a conductor. We considered in this case an highly conductive wire (σ = 1e7 S/m) of rectangular cross section enclosed in square shape with axis of symmetry directed toward $\hat{\boldsymbol{y}}$. After exciting the structure with a plane wave traveling along $\hat{\boldsymbol{y}}$, the resulting current density distribution in a cross section of the line at z = 0 m is shown in Fig. 9 for different frequencies of the impinging wave. Despite the use of the preconditioning strategy tailored for inductive magnetic frill excitations, the solution is expected to be accurate even in presence of plane wave excitations if the operating frequency is not extremely low. We notice that the visible penetration length, which decreases when increasing the frequency, is comparable with the skin depth δ, which is also reported in the figures as the black lines for ease of comparison.

VII. Conclusion

In this work, we presented a novel full-wave formulation amenable to eddy-current simulations in circuital frameworks. Built upon the PMCHWT integral equation, it results from a quasi-Helmholtz preconditioning strategy of projective type. With respect to the standard loop-star decomposition, the quasi-Helmholtz projectors offer several advantages, including their compatibility with fast solvers and acceleration strategies and their lack of detrimental effect on the condition number with respect to dense discretizations. The proposed preconditioning strategy offers the twofold advantage of curing the frequency and conductivity instabilities of the original formulation, including the severe low-frequency breakdown preventing its application toward statics, and curing the typical loss of accuracy occurring at very low-frequency. The resulting scheme is well-conditioned and stable for materials ranging from dielectric to highly conductive, applicable to both simply and multiply-connected structures and prone to seamless transitions between lower to higher frequencies. Although the proposed scheme provides optimal accuracy in presence of magnetic frill-type excitations, the procedure employed in defining the proposed preconditioning strategy can also be applied to other types of excitations, which will be topic of future investigations.

References

[1] C. A. Balanis, *Advanced Engineering Electromagnetics*, 2nd ed., Hoboken, NJ, USA: Wiley, 2012.

[2] H. K. Dirks, "Quasi-stationary fields for microelectronic applications," *Electr. Eng.*, vol. 79, no. 2, pp. 145–155, Apr. 1996.

[3] S. Sauter and C. Schwab, *Boundary Element Methods* (Springer Series in Computational Mathematics), vol. 39, Berlin, Germany: Springer, 2011.

[4] O. Steinbach, *Numerical Approximation Methods for Elliptic Boundary Value Problems: Finite and Boundary Elements*. New York, NY, USA: Springer, 2008.

[5] A. Poggio and E. Miller, "Integral equation solutions of three-dimensional scattering problems," in *Computer Techniques for Electromagnetics*. Amsterdam, The Netherlands: Elsevier, 1973, pp. 159–264.

[6] C. Müller, "Grundprobleme der mathematischen theorie elektromagnetischer schwingungen," *Amer. Math. Monthly*, vol. 65, p. 459, Jun. 1958.

[7] I. Bogaert, K. Cools, F. Andriulli, and H. Bagci, "Low-frequency scaling of the standard and mixed magnetic field and Müller integral equations," *IEEE Trans. Antennas Propag.*, vol. 62, no. 2, pp. 822–831, Feb. 2014.

[8] P. Ylä-Oijala, M. Taskinen, and S. Järvenpää, "Analysis of surface integral equations in electromagnetic scattering and radiation problems," *Eng. Anal. Boundary Elements*, vol. 32, no. 3, pp. 196–209, Mar. 2008.

[9] E. van't Wout, S. R. Haqshenas, P. Gélat, T. Betcke, and N. Saffari, "Boundary integral formulations for acoustic modelling of high-contrast media," *Comput. Math. Appl.*, vol. 105, pp. 136–149, Jan. 2022.

[10] S. B. Adrian, A. Dély, D. Consoli, A. Merlini, and F. P. Andriulli, "Electromagnetic integral equations: Insights in conditioning and preconditioning," *IEEE Open J. Antennas Propag.*, vol. 2, pp. 1143–1174, 2021.

[11] K. Cools, F. Andriulli, and E. Michielssen, "A Calderón multiplicative preconditioner for the PMCHWT integral equation," *IEEE Trans. Antennas Propag.*, vol. 59, no. 12, pp. 4579–4587, Dec. 2011.

[12] Y. Beghein, R. Mitharwal, K. Cools, and F. P. Andriulli, "On a low-frequency and refinement stable PMCHWT integral equation leveraging the quasi-Helmholtz projectors," *IEEE Trans. Antennas Propag.*, vol. 65, no. 10, pp. 5365–5375, Oct. 2017.

[13] R. Hiptmair, "Boundary element methods for eddy current computation," in *Boundary Element Analysis*, vol. 29, M. Schanz and O. Steinbach, Eds., Berlin, Germany: Springer, 2007, pp. 213–248.

[14] E. Kriezis, T. Tsiboukis, S. Panas, and J. Tegopoulos, "Eddy currents: Theory and applications," *Proc. IEEE*, vol. 80, no. 10, pp. 1559–1589, Oct. 1992.

[15] J. García-Martín, J. Gómez-Gil, and E. Vázquez-Sánchez, "Non-destructive techniques based on eddy current testing," *Sensors*, vol. 11, no. 3, pp. 2525–2565, Feb. 2011.

[16] W. M. Rucker, R. Hoschek, and K. R. Richter, "Various BEM formulations for calculating eddy currents in terms of field variables," *IEEE Trans. Magn.*, vol. 31, no. 3, pp. 1336–1341, May 1995.

[17] K. Niino and N. Nishimura, "Calderón preconditioning approaches for PMCHWT formulations for Maxwell's equations," *Int. J. Numer. Model., Electron. Netw., Devices Fields*, vol. 25, pp. 558–572, Sep. 2012.

[18] S. Yan, J.-M. Jin, and Z. Nie, "A comparative study of Calderón preconditioners for PMCHWT equations," *IEEE Trans. Antennas Propag.*, vol. 58, no. 7, pp. 2375–2383, Jul. 2010.

[19] T. L. Chhim, A. Merlini, L. Rahmouni, J. E. O. Guzman, and F. P. Andriulli, "Eddy current modeling in multiply connected regions via a full-wave solver based on the quasi-Helmholtz projectors," *IEEE Open J. Antennas Propag.*, vol. 1, pp. 534–548, 2020.

[20] F. P. Andriulli, K. Cools, I. Bogaert, and E. Michielssen, "On a well-conditioned electric field integral operator for multiply connected geometries," *IEEE Trans. Antennas Propag.*, vol. 61, no. 4, pp. 2077–2087, Apr. 2013.

[21] F. P. Andriulli, "Loop-star and loop-tree decompositions: Analysis and efficient algorithms," *IEEE Trans. Antennas Propag.*, vol. 60, no. 5, pp. 2347–2356, May 2012.

[22] W. Hackbusch, "A sparse matrix arithmetic based on $\mathcal{H}$-matrices. Part I: Introduction to $\mathcal{H}$-matrices," *Computing*, vol. 62, pp. 89–108, Apr. 1999.

[23] W. Hackbusch and B. N. Khoromskij, "A sparse $\mathcal{H}$-matrix arithmetic. Part II: Application to multi-dimensional problems," *Computing*, vol. 64, pp. 21–47, Feb. 2000.

[24] I. Bogaert, K. Cools, F. P. Andriulli, and D. De Zutter, "Low frequency scaling of the mixed MFIE for scatterers with a non-simply connected surface," in *Proc. Int. Conf. Electromagn. Adv. Appl.*, Sep. 2011, pp. 951–954.

[25] Z. Guo Qian, W. Cho Chew, and R. Suaya, "Generalized impedance boundary condition for conductor modeling in surface integral equation," *IEEE Trans. Microw. Theory Techn.*, vol. 55, no. 11, pp. 2354–2364, Nov. 2007.

[26] A. Quarteroni and A. Valli, *Numerical Approximation of Partial Differential Equations* (Springer Series in Computational Mathematics), vol. 23, Berlin, Germany: Springer, 2008.

[27] H. V. Henderson and S. R. Searle, "On deriving the inverse of a sum of matrices," *SIAM Rev.*, vol. 23, no. 1, pp. 53–60, Jan. 1981.
[28] L. Tsai, "A numerical solution for the near and far fields of an annular ring of magnetic current," *IEEE Trans. Antennas Propag.*, vol. AP-20, no. 5, pp. 569–576, Sep. 1972.
[29] B. Popović, M. B. Dragović, and A. R. Djordjević, *Analysis and Synthesis of Wire-Antennas* (Electronic & Electrical Engineering Research Studies), no. 2, New York, NY, USA: Research Studies Press, 1982.
[30] R. P. Feynman, *The Feynman Lectures on Physics. Volume 1: Mainly Mechanics, Radiation, and Heat*. New York, NY, USA: Basic Books, 2011.
[31] C. R. Paul, *Inductance: Loop and Partial*. Hoboken, NJ, USA: Wiley, 2010.

Viviana Giunzioni (Member, IEEE) received the Laurea degree in electronic and communications engineering, the Master of Science degree in electronic engineering, and the Ph.D. degree in electrical, electronics, and communications engineering from the Politecnico di Torino, Turin, Italy, in 2019, 2021, and 2025, respectively.

Since 2021, she has been a Research Associate with the Politecnico di Torino. Her research interests include computational electromagnetics, focusing on preconditioning techniques and fast solvers for integral equations.

Dr. Giunzioni received an Honorable Mention at the IEEE Antennas and Propagation Symposium (IEEE AP-S) in 2022 and another Honorable Mention at the URSI General Assembly and Scientific Symposium (URSI GASS) in 2023. In 2024, she was a Finalist for the Young Scientist Award from the International Conference on Electromagnetics in Advanced Applications (ICEAA-IEEE APWC). In 2025, she received the Young Scientist Award from the URSI International Symposium on Electromagnetic Theory (EMTS).

Alberto Scazzola (Member, IEEE) received the master's degree in physics from the University of Trieste, Trieste, Italy, in 2018, and the Ph.D. degree in theory and numerical simulation of condensed matter from SISSA, Trieste, in 2022.

His Ph.D. work involved research on high-temperature superconductivity. From 2022 to 2024, he was a Research Fellow from the CERL Team, Politecnico di Torino, Turin, Italy. He is currently working as a High-School Teacher. His research interests include computational electromagnetics and computational physics, involving the development of libraries and the implementation of numerical methods.

Adrien Merlini (Senior Member, IEEE) received the M.Sc.Eng. degree from the École Nationale Supérieure des Télécommunications de Bretagne (Télécom Bretagne), Rennes, France, in 2015, and the Ph.D. degree from the École Nationale Supérieure Mines-Télécom Atlantique (IMT Atlantique), Brest, France, in 2019.

From 2018 to 2019, he was a Visiting Ph.D. Student from the Politecnico di Torino, Turin, Italy, which he then joined as a Research Associate. Since 2019, he has been an Associate Professor with the Microwave Department, IMT Atlantique. He is currently a member of the Lab-STICC Laboratory. His research interests include preconditioning and acceleration of integral equation solvers for electromagnetic simulations and their application to brain imaging.

Dr. Merlini is a member of IEEE-HKN, the IEEE Antennas and Propagation Society, and URSI France. He received the Young Scientist Award from the URSI GASS 2020 and the EMTS 2023 meetings. He authored and co-authored award-winning papers, including the Third Place at the EMTS 2023 Best Paper Competition, the Best Paper Award from the 2022 ICEAA-IEEE APWC Conference, five papers that received honorable mentions (URSI/IEEE-APS 2021, 2022, and 2023), and three best paper finalists (URSI GASS 2020, and URSI/IEEE-APS 2021 and 2022). He is serving as an Associate Editor and an Editor of the Open Source Column for *IEEE Antennas and Propagation Magazine*.

Francesco P. Andriulli (Fellow, IEEE) received the Laurea degree in electrical engineering from Politecnico di Torino, Turin, Italy, in 2004, the M.Sc. degree in electrical engineering and computer science from the University of Illinois at Chicago, Chicago, IL, USA, in 2004, and the Ph.D. in electrical engineering from the University of Michigan at Ann Arbor, Ann Arbor, MI, USA, in 2008.

From 2008 to 2010, he was a Research Associate with the Politecnico di Torino. From 2010 to 2017, he was an Associate Professor (2010-2014) and then a Full Professor with the École Nationale Supérieure Mines-Télécom Atlantique (IMT Atlantique), Brest, France. Since 2017, he has been a Full Professor with the Politecnico di Torino. His research interests are in computational electromagnetics including frequency- and time-domain integral equation solvers, well-conditioned formulations, fast solvers, low-frequency electromagnetic analyses, and modeling techniques for antennas, wireless components, microwave circuits, and biomedical applications with a special focus on brain imaging.

Prof. Andriulli received several best paper awards at conferences and symposia (URSI NA 2007, IEEE AP-S 2008, ICEAA IEEE-APWC 2015) also in co-authorship with his students and collaborators (ICEAA IEEE-APWC 2021, EMTS 2016, URSI-DE Meeting 2014, ICEAA 2009) with whom received also a second prize conference paper (URSI GASS 2014), a third prize conference paper (IEEE-APS 2018), seven honorable mention conference papers (ICEAA 2011, URSI/IEEE-APS 2013, 4 in URSI/IEEE-APS 2022, URSI/IEEE-APS 2023) and other three finalist conference papers (URSI/IEEEAPS 2012, URSI/IEEE-APS 2007, URSI/IEEE-APS 2006, URSI/IEEE-APS 2022)). Moreover, he received the 2014 IEEE AP-S Donald G. Dudley Jr. Undergraduate Teaching Award, the triennium 2014-2016 URSI Issac Koga Gold Medal, and the 2015 L. B. Felsen Award for Excellence in Electrodynamics. He received the International Union of Radio Science (URSI), and a member of Eta Kappa Nu, Tau Beta Pi, and Phi Kappa Phi. He is the Editor-in-Chief of the IEEE *Antennas and Propagation Magazine*, he serves as a Track Editor for the IEEE TRANSACTIONS ON ANTENNAS AND PROPAGATION, and as an Associate Editor of *URSI Radio Science Letters*. He served as an Associate Editor for the IEEE ANTENNAS AND WIRELESS PROPAGATION LETTERS, IEEE ACCESS, and IETMAP.